Mapping the Pulsar Environment with Pulsed Fraction Spectroscopy

Antonino D'Aì (IASF Palermo)
D. K. Maniadakis, E. Ambrosi, G. Cusumano, C. Ferrigno (Uni Genève), E.Sokolova-Lapa, P. Kretchmar, F. Furst and many others

Talk Outline: what pulse profiles tell us

> Research objectives and methods

> Energy-resolved pulse profiles as spectroscopic diagnostic tool

> Application of these methods to a sample of **HMXB**

> Future directions

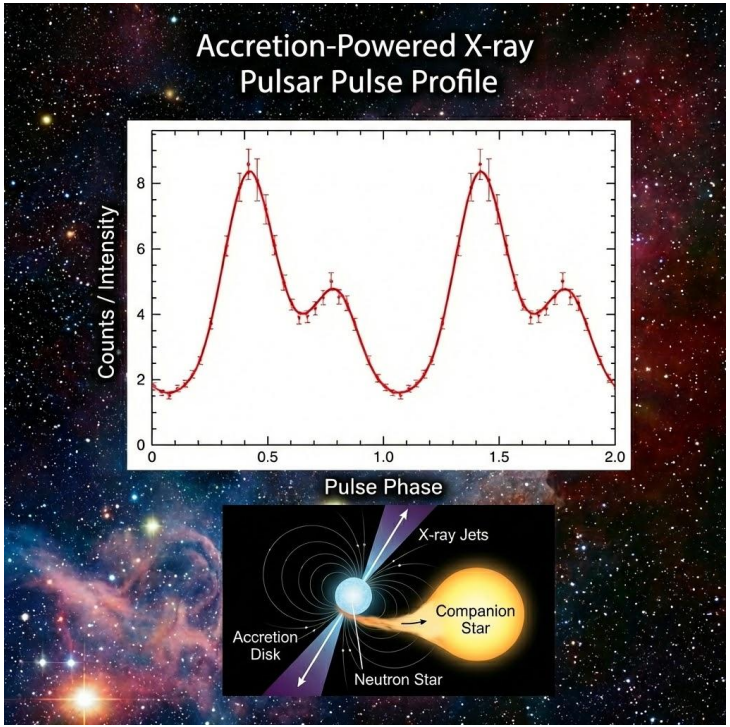

Methodology

Pulse profiles have been widely studied ...

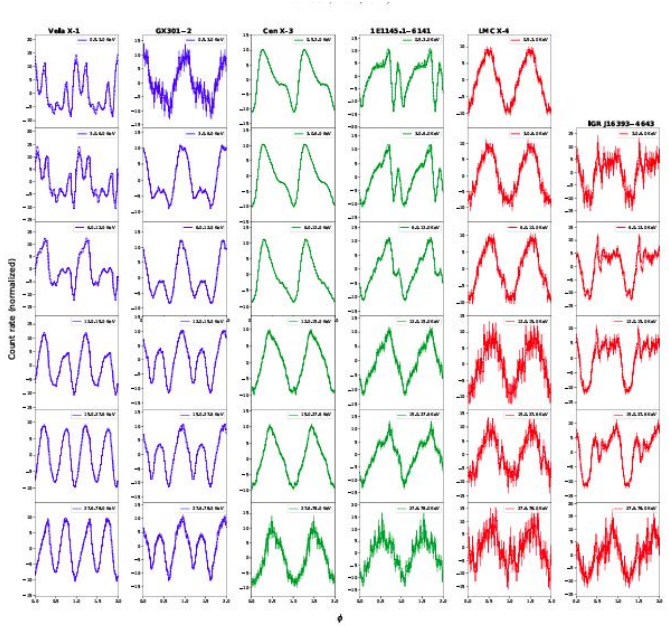

Fig. 3. Comparison of the normalized pulse profiles of different sources of the sample studied at different energy ranges. The sources are in order from *left to right*: Vela X−1 (type 2), GX 301 − 2 (type 2), Cen X−3 (type 1), 1E1145.1−6141 (type 1), LMC X−4 (type 0), and IGR J16393−4643 (type 0). The measured profiles are represented by solid lines, whereas the Fourier fits are represented by dashed lines. The boundaries of the energy ranges are [0.5, 3, 6, 12, 15, 27.6, and 78] keV. The pulse profiles were phase shifted by hand to align the maximums of the pulse profiles of two observations (in cases with observations of both telescopes) and coloured according to their respective pulse profile types in order to better show a comparison between them.

Alonso-Hernandez, 2022

Pulse profiles have been widely studied

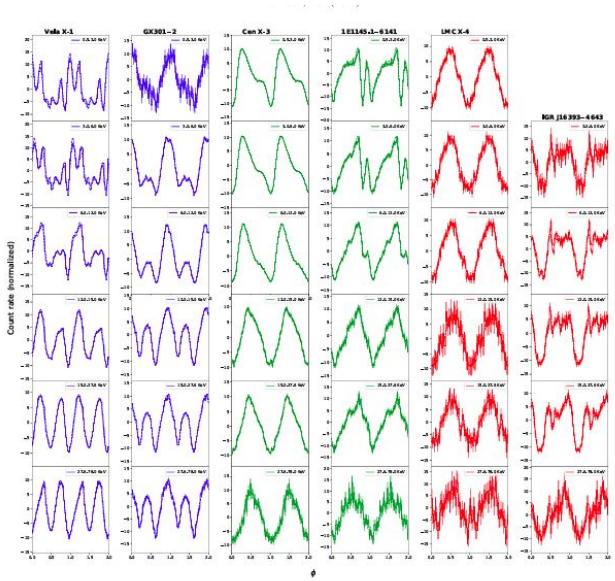

Fig. 3. Comparison of the normalized pulse profiles of different sources of the sample studied at different energy ranges. The sources are in order from *left to right*: Vela X−1 (type 2), GX 301 − 2 (type 2), Cen X−3 (type 1), 1E1145.1−6141 (type 1), LMC X−4 (type 0), and IGR J16393−4643 (type 0). The measured profiles are represented by solid lines, whereas the Fourier fits are represented by dashed lines. The boundaries of the energy ranges are [0.5, 3, 6, 12, 15, 27.6, and 78] keV. The pulse profiles were phase shifted by hand to align the maximums of the pulse profiles of two observations (in cases with observations of both telescopes) and coloured according to their respective pulse profile types in order to better show a comparison between them.

Alonso-Hernandez, 2022

Energy dependence of the pulsed fraction

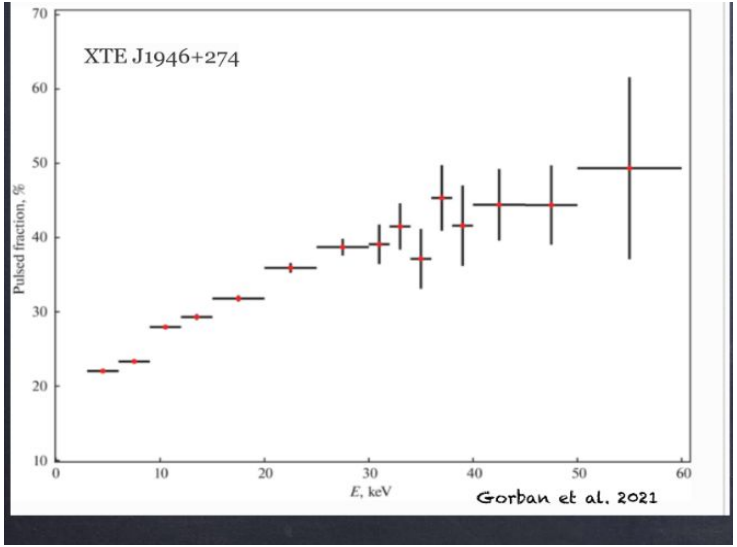

The close and distant pulsar environments

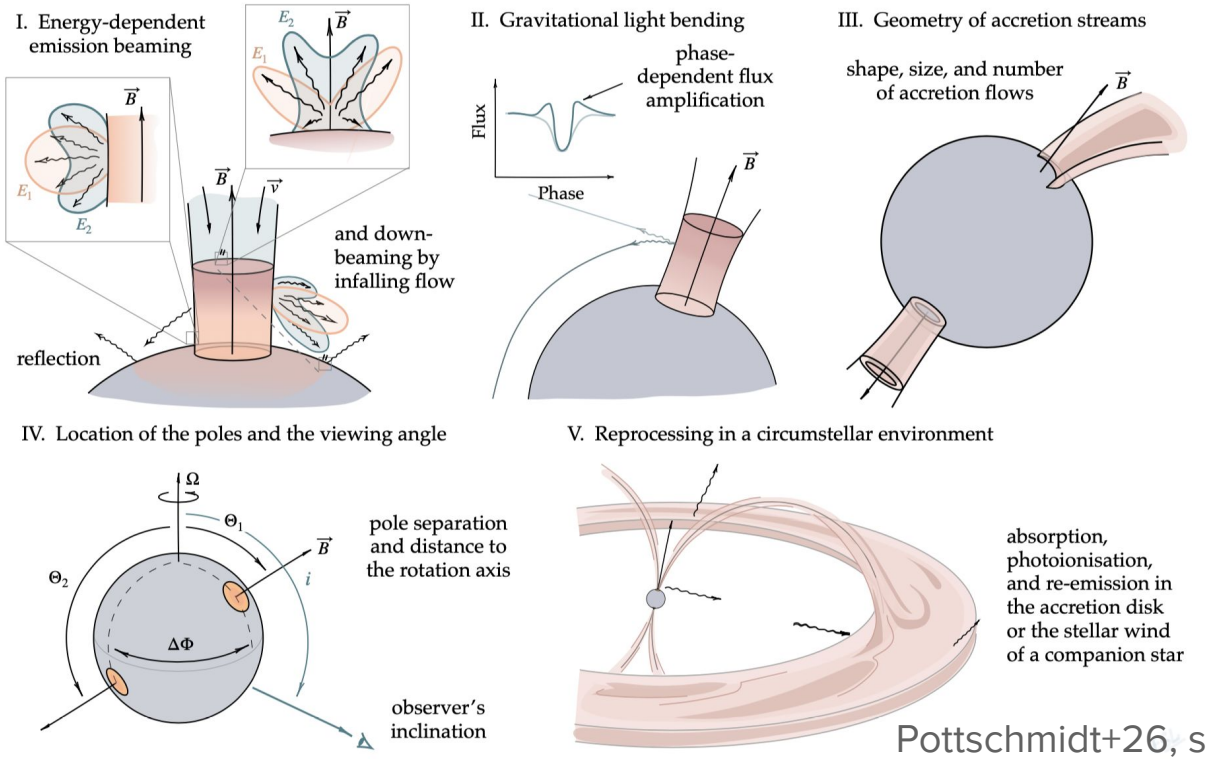

Pottschmidt+26, submitted

Cyclotron resonant scattering features in the energy spectra of accreting X-ray pulsars

The absorption cyclotron line in AXP is caused by resonant absorption and scattering of photons between Landau levels.

Abrupt changes in the pulsed fraction at the fundamental cyclotron energy have been previously reported in several sources.

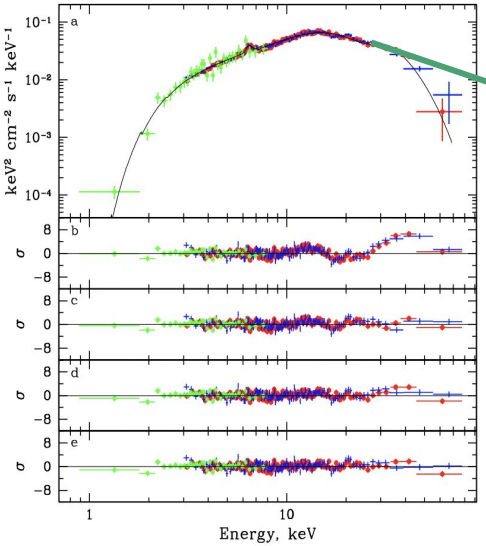

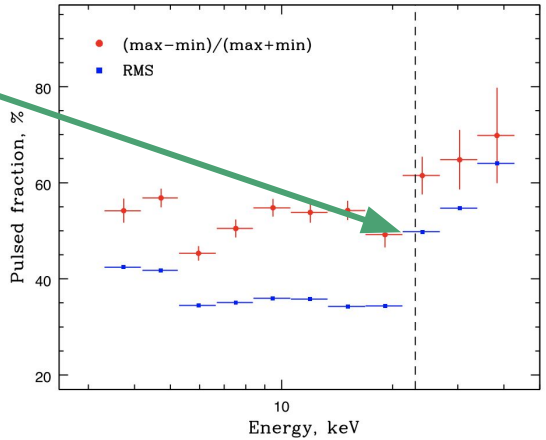

Figure 5. Dependence of the pulsed fraction of IGR J18027−2016 on energy calculated in two different ways (see the text for details). The dashed line shows the position of the cyclotron line that may be present in the source spectrum.

Lutovinov+2017
doi: 10.1093/mnras/stw3058

Research objectives

- Create a “catalogue” of energy-resolved pulse profiles based on **NuSTAR** data for all pulsars which have a clear cyclotron line detection.
- A database with uniform, easily cross-checkable, timing products.
- **Study the amplitude energy dependence in conjunction with spectroscopic results**
- Test and compare results from benchmark sources
- Exploit all the accessible parameter space from pulse profile decomposition.

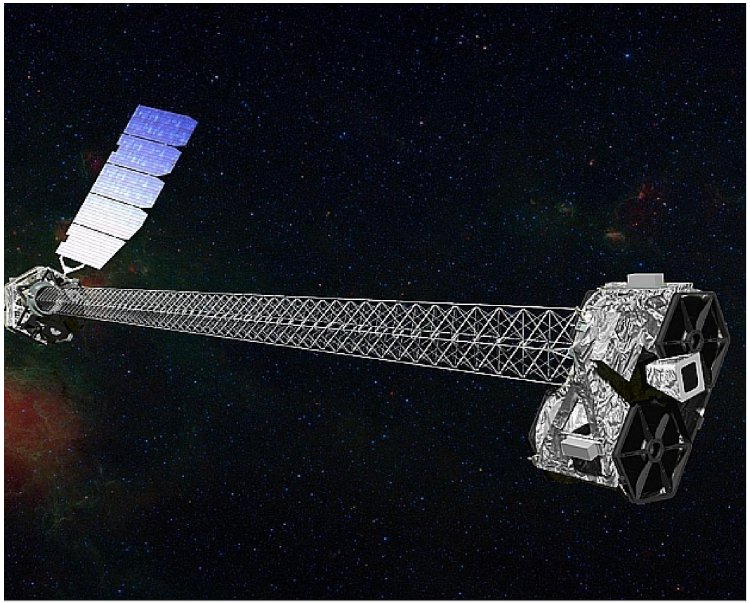

Methods: a pipeline for automatic analysis of PP

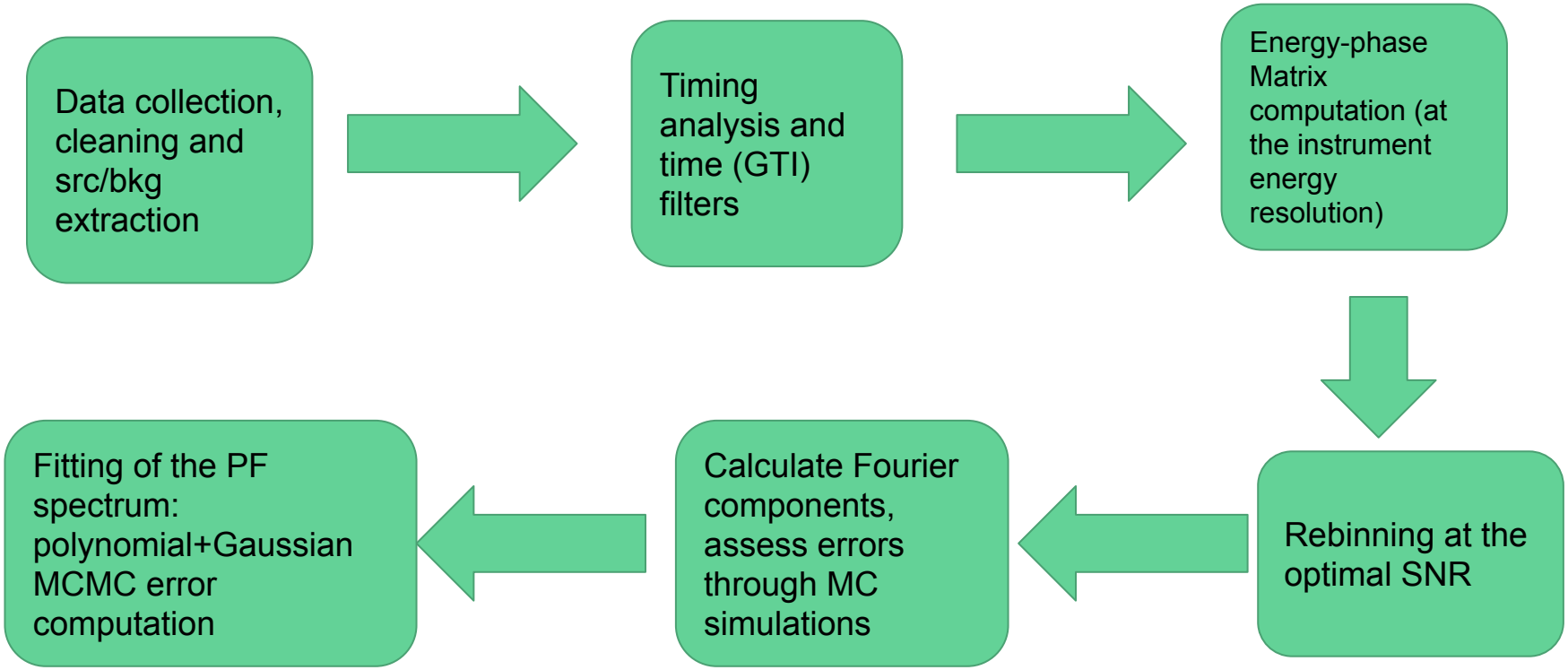

Methods: a pipeline for automatic analysis of PP

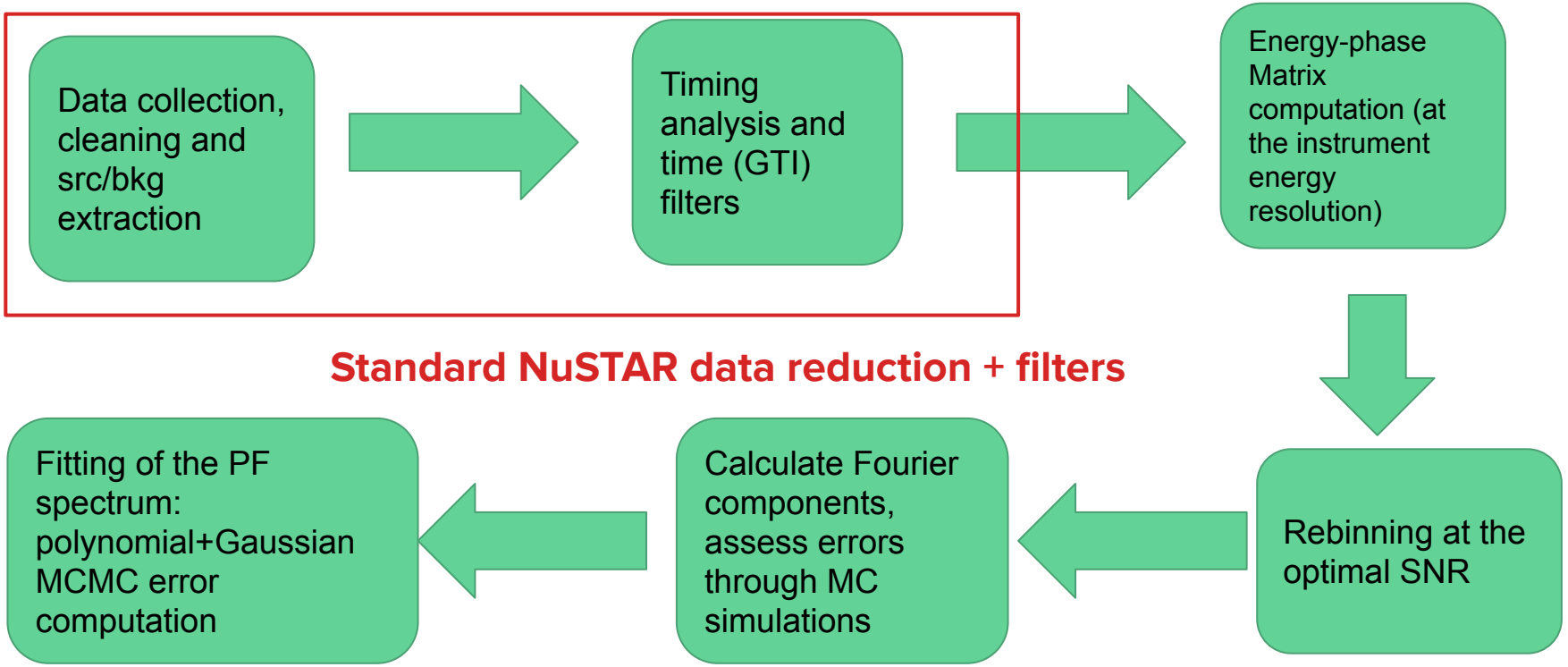

Methods: a pipeline for automatic analysis of PP

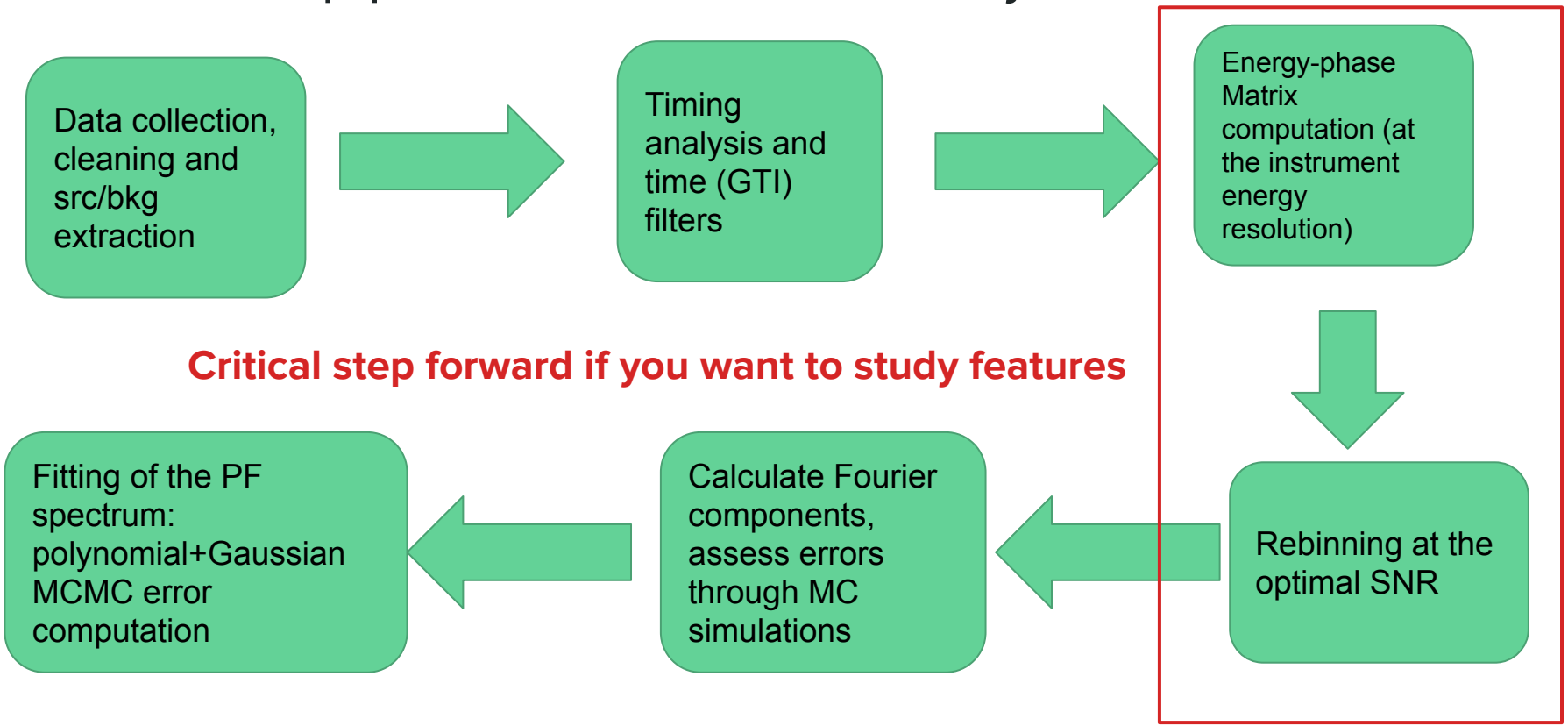

Energy-phase matrices

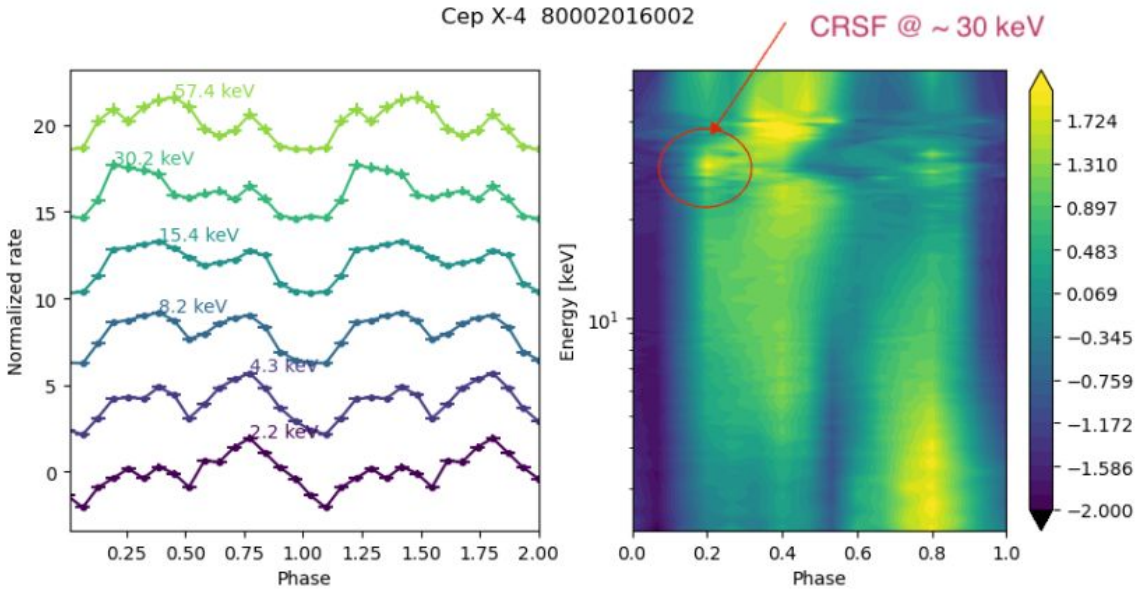

Fig. 12 Representative energy-selected pulse profiles (left, offset for visualization) of the full phase-energy map (right) for a *NuSTAR* observation of Cep X-4. The map shows a clear discontinuity in the energy range associated with the presence of a cyclotron resonance scattering feature. It also highlights the strong energy dependence of the amplitude of the peak at phase ~0.8. Adapted from Ferrigno et al. (2023).

Methods: a pipeline for automatic analysis of PP

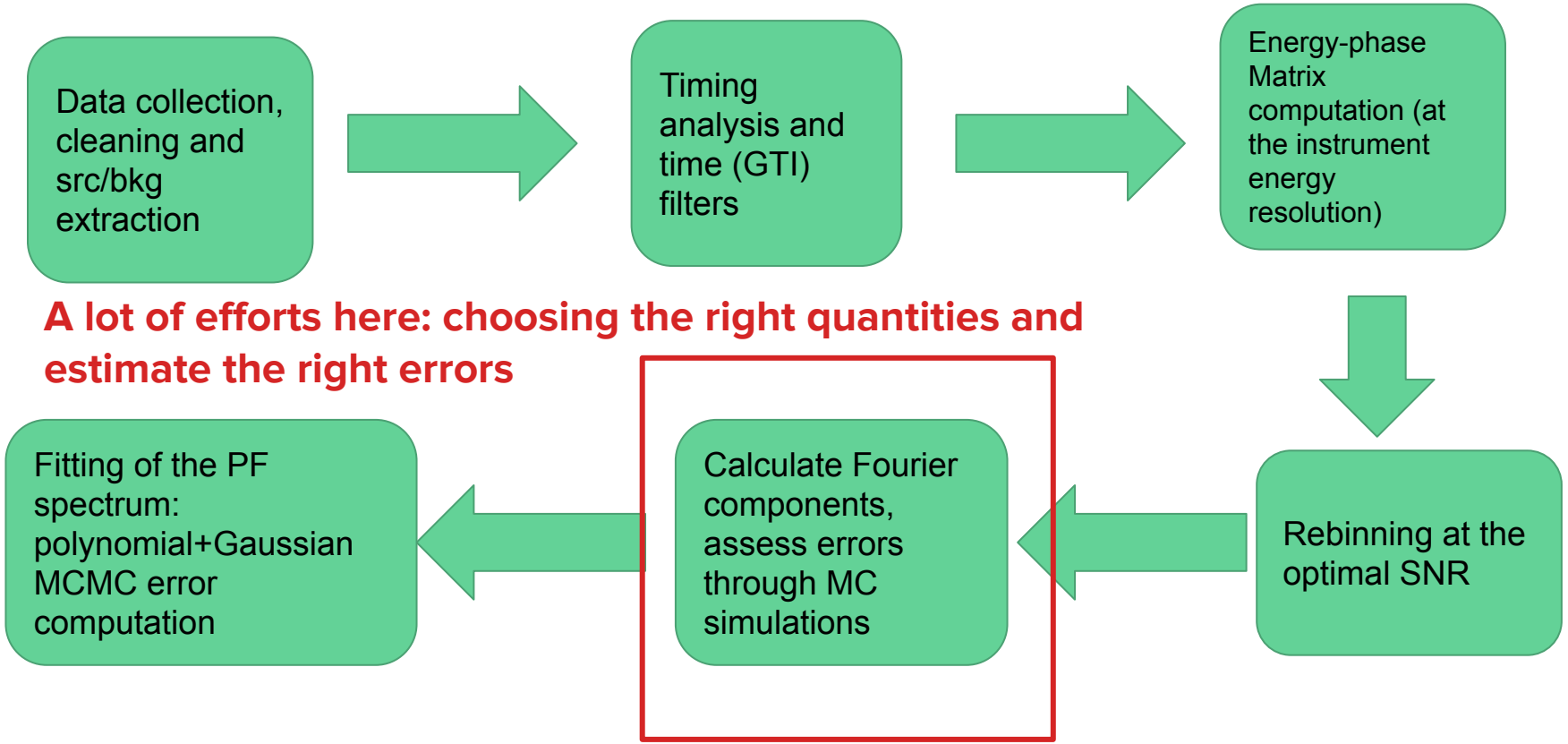

What is meant by **pulsed fraction (PF)**?

No general consensus, but always understood as the power of the modulated signal. It can be normalised with respect to the total observed emission (that's why it is a fraction). But the "*exact numeric value*" can be known only in the limit of very high statistics. In general "the PF value" depends a lot on the method and on the user-defined binning of the pulse profile.

$$\mathrm{PF}_{\mathrm{area}} = \frac{1}{\sum_{j=1}^{N_{\mathrm{bin}}} C_j} \sum_{j=1}^{N_{\mathrm{bin}}} (C_j - C_{\mathrm{min}}).$$

$$\mathrm{PF}_{\mathrm{minmax}} = \frac{C_{\mathrm{max}} - C_{\mathrm{min}}}{C_{\mathrm{max}} + C_{\mathrm{min}}}.$$

$$\mathrm{PF}_{\mathrm{fit}} = \frac{\int_0^1 (f(\phi) - C_{\mathrm{min}})\, d\phi}{\int_0^1 f(\phi)\, d\phi}.$$

$$\mathrm{PF}_{\mathrm{FFT}} = \frac{1}{a_0} \sqrt{2 \sum_{k=1}^{N_{\mathrm{harm}}} \left[(a_k^2 + b_k^2) - (\sigma_{a_k}^2 + \sigma_{b_k}^2) \right]}.$$

$$\mathrm{PF}_{\mathrm{RMS}} = \frac{1}{C_{\mathrm{avg}}} \sqrt{\frac{\Sigma_{j=1}^{N_{\mathrm{bin}}} \left[(C_i - C_{\mathrm{avg}})^2 - \sigma_{C_i}^2 \right]}{N_{\mathrm{bin}}}}$$

Not all the definitions are equally effective

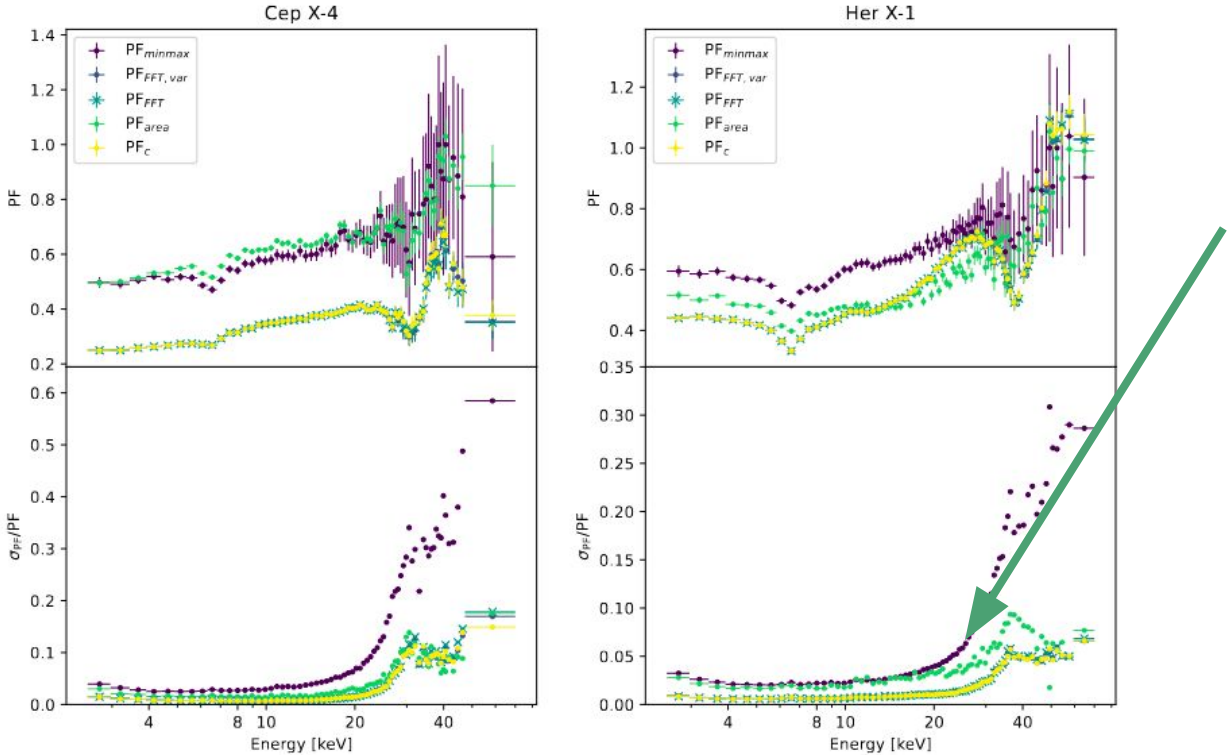

At low statistics some definitions result in much larger uncertainty, which comes not from data but on the definition itself.

Ferrigno, D'Aì, Ambrosi, A&A, 2023

So the PF values are method-dependent?

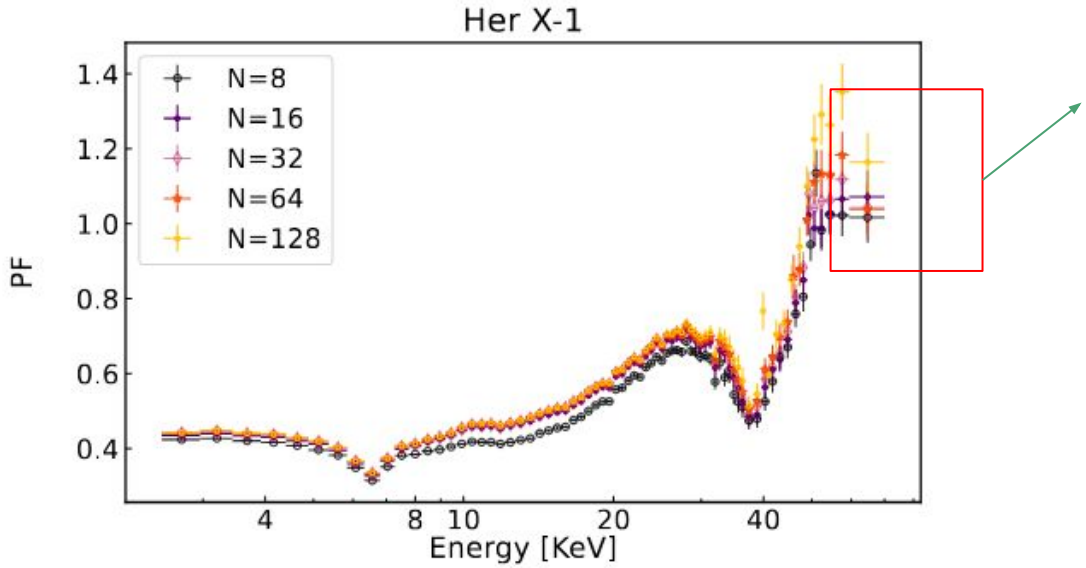

Fig. A.3. PF_{FFT} obtained with different N_{bins} for the pulse profile of Her X −1 analyzed in this work.

FFT/RMS methods can slightly go even above 1. They are not really “fractions”.

But they offer the advantage to be less biased against the Nbins choice and to have the minimum relative uncertainty.

Ferrigno, D’Aì, Ambrosi, A&A, 2023

Methods: a pipeline for automatic analysis of PP

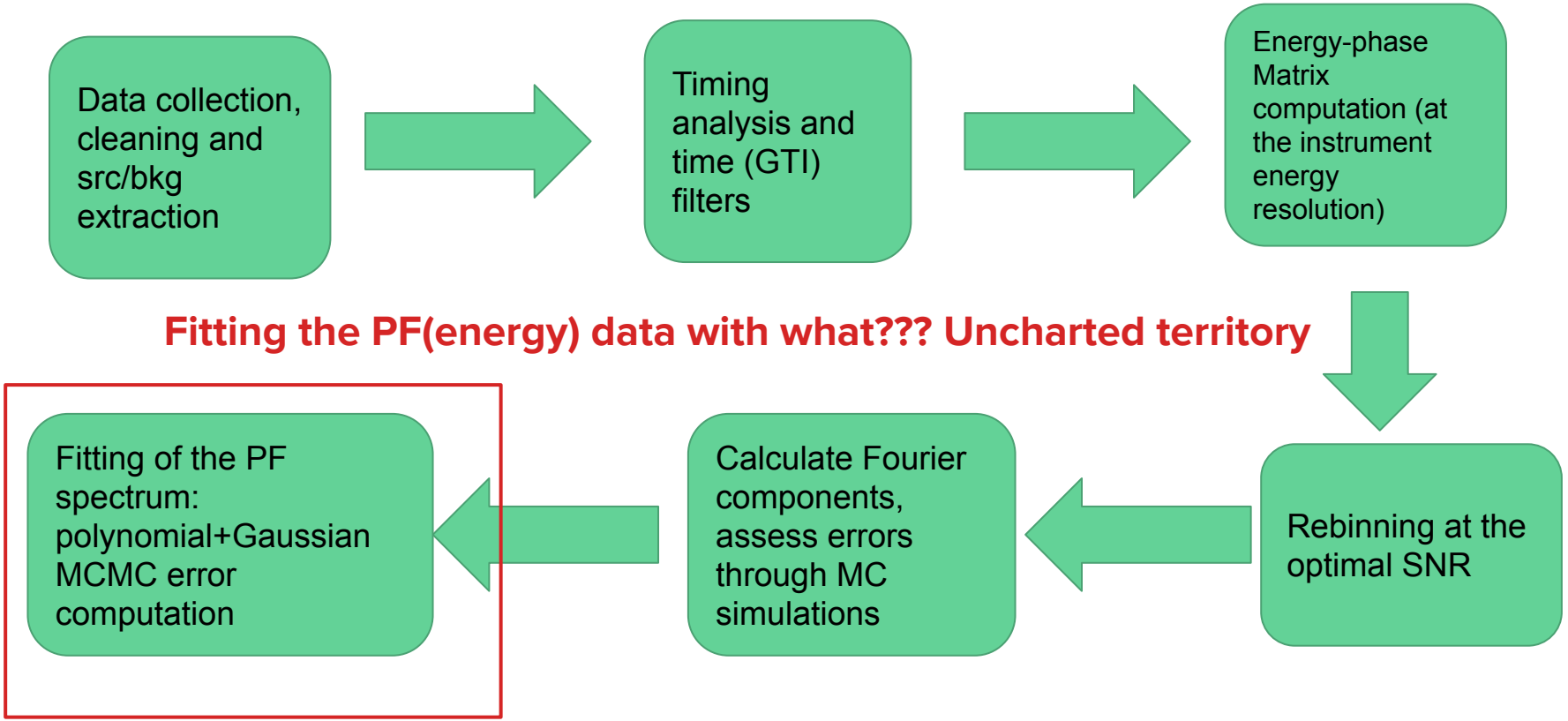

Giving quantitative estimates

The key objective in decomposing the PPs was to pass from qualitative descriptions to quantitative estimates. To give numbers and errors associated with.
Treat the PF values vs energy as it were a “**energy spectrum**”.
We called it the **Pulsed Fraction Spectrum (PFS)**

Giving quantitative estimates

The key point in decomposing the PPs was to pass from qualitative descriptions to quantitative estimates. To give numbers and errors associated with.
Treat the PF values vs energy as it were a “**energy spectrum**”. We called it the **Pulsed Fraction Spectrum (PFS)**

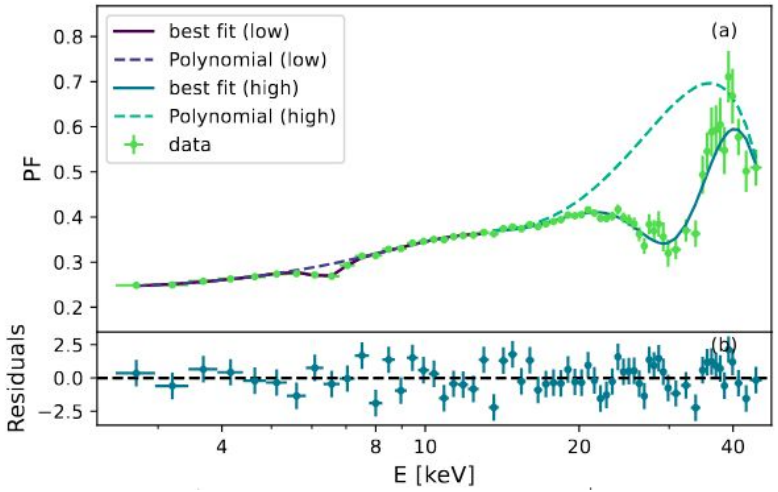

Phenomenological approach:

- use polynomials for the continuum (raise the polynomial degree until the description is ok)
- use Gaussians for the features
- split the energy range to avoid too high n-polynomials
- use MCMC for error estimates

Pulsed fraction as a spectroscopic diagnostic tool

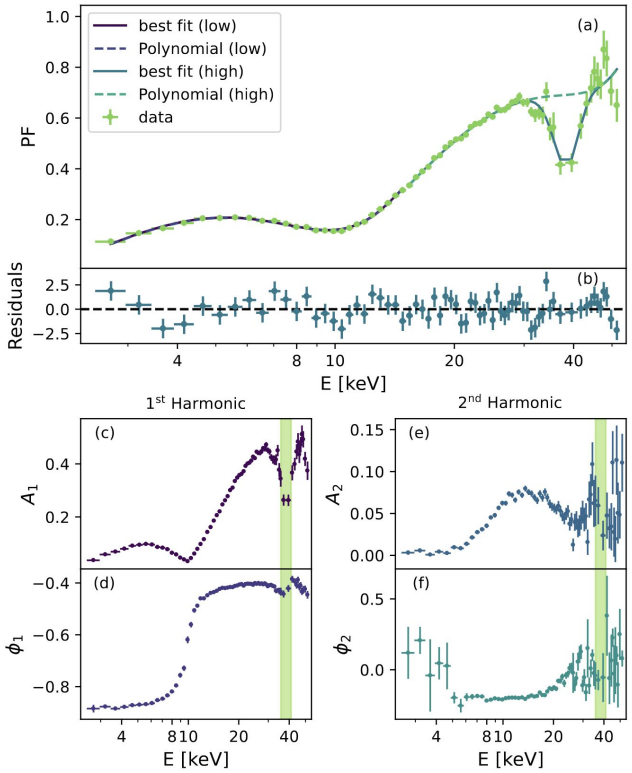

Table 2. Best-fit parameters of the 4U 1626-67 ObsID 30101029002 pulse and amplitude models compared to spectral results. The last column values from the spectral best-fit of the same data set (see Model BWM3 of Table 1 in D'Aì et al. 2017).

	PF	1st	Spectral	
$\chi^2_{red,lo}$/d.o.f.	1.1/17	1.6/13	—	
$\chi^2_{red,hi}$/d.o.f.	1.4/40	1.1/40	—	
$n_{pol}^{(lo)}$	4	6	—	
$n_{pol}^{(hi)}$	3	5	—	
E_{split}	13.21	12.33	—	keV
A_{Cyc}	-2.16±0.14	$-2.2^{+0.2}_{-0.3}$	23.0±0.9	
E_{Cyc}	38.29±0.15	39.07±0.19	37.90±0.15	keV
σ_{Cyc}	3.06±0.20	3.6±0.2	6.0±0.3	keV

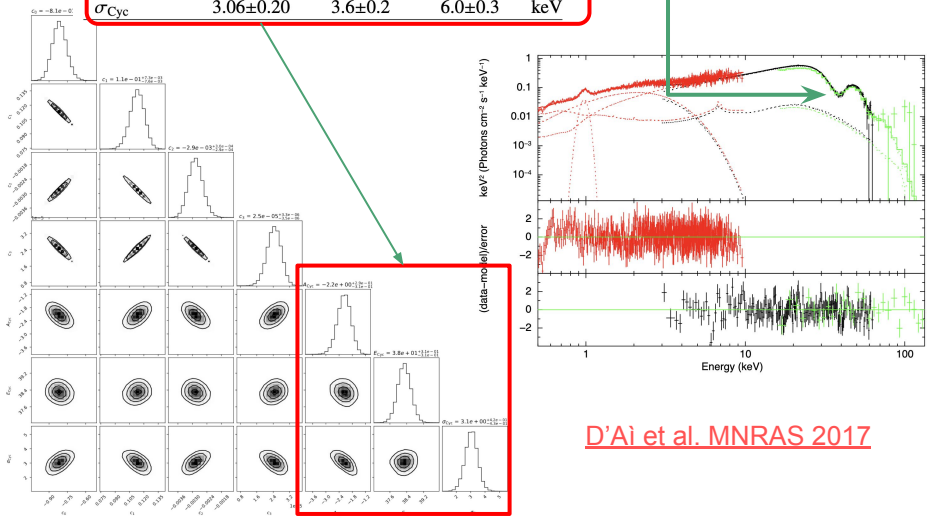

D'Aì et al. MNRAS 2017

Other examples from Ferrigno, D'Aì, Ambrosi (A&A 2023)

Cep X-4

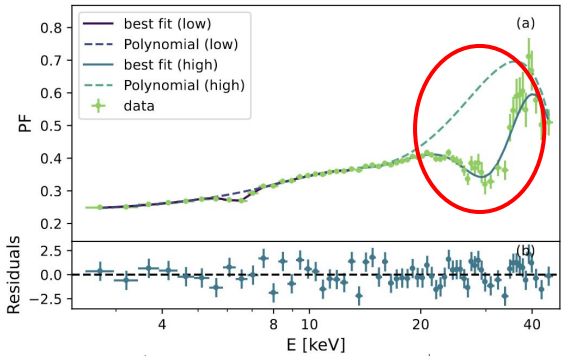

	PF	1st	Spectral	
$\chi^2_{\rm red,lo}$/d.o.f.	1.4/15	0.8/8	—	
$\chi^2_{\rm red,hi}$/d.o.f.	1.5/35	1.3/39	—	
$n_{\rm pol}^{\rm (lo)}$	3	6	—	
$n_{\rm pol}^{\rm (hi)}$	3	3	—	
$E_{\rm split}$	13.35	11.18	—	keV
$A_{\rm Fe}$	-0.0308±0.0019	(-8±2) ×10^{-3}	(1.39±0.16) ×10^{-3}	
$E_{\rm Fe}$	6.444±0.019	6.62±0.04	6.47±0.03	keV
$\sigma_{\rm Fe}$	0.46±0.02	0.33±0.05	0.42±0.05	keV
$A_{\rm Cyc}$	-4.1±0.7	-2.08±0.12	20^{+5}_{-4}	
$E_{\rm Cyc}$	31.00±0.18	30.32±0.10	$30.39^{+0.17}_{-0.14}$	keV
$\sigma_{\rm Cyc}$	5.3±0.3	3.75±0.12	5.8±0.4	keV

Cen X-3

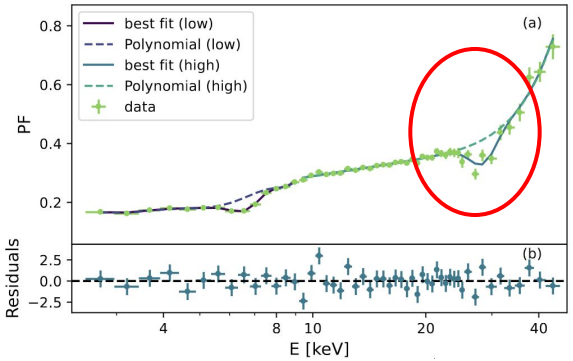

	PF	1st	2nd	Spectral	
$\chi^2_{\rm red,lo}$/d.o.f.	1.6/4	2.0/8	0.8/17	—	
$\chi^2_{\rm red,hi}$/d.o.f.	1.3/31	2.1/27	1.1/24	—	
$n_{\rm pol}^{\rm (hi)}$	3	7	1	—	
$n_{\rm pol}^{\rm (lo)}$	6	2	2	—	
$E_{\rm split}$	9.40	9.40	13.78	—	keV
$A_{\rm Fe}$	$-0.09^{+0.02}_{-0.03}$	-0.0239±0.0018	-0.0271±0.0015	$0.117^{+0.007}_{-0.011}$	
$E_{\rm Fe}$	6.69±0.04	6.42±0.02	6.55±0.03	6.67^a	keV
$\sigma_{\rm Fe}$	0.64±0.06	0.47±0.03	0.56±0.03	0.53^a ±0.03	keV
$A_{\rm Cyc}$	-0.53±0.08	$0.04^{+0.15}_{-0.04}$	-1.68±0.12	0.40±0.13	
$E_{\rm Cyc}$	28.8±0.3	29^{+3}_{-3}	28.5±0.3	30.3±0.6	keV
$\sigma_{\rm Cyc}$	2.5±0.3	5±1	7.2±0.3	5.0±0.9	keV

Her X-1

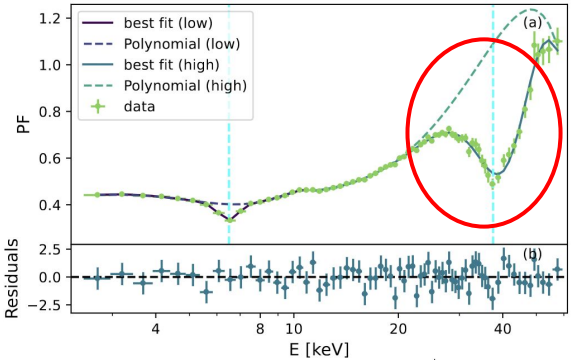

	PF	1st	2nd	Spectral	
$\chi^2_{\rm red,lo}$/d.o.f.	0.7/10	0.5/10	1.5/14	—	
$\chi^2_{\rm red,hi}$/d.o.f.	1.0/47	1.2/47	1.2/45	—	
$n_{\rm pol}^{\rm (lo)}$	4	4	3	—	
$n_{\rm pol}^{\rm (hi)}$	3	3	2	—	
$E_{\rm split}$	11.17	11.01	12.82	—	keV
$A_{\rm Fe}$	-0.072±0.002	-0.0486±0.0016	$-0.019^{+0.003}_{-0.004}$	(6.3±0.7) ×10^{-3}	
$E_{\rm Fe}$	6.503±0.008	6.524±0.008	6.51±0.05	6.55±0.05	keV
$\sigma_{\rm Fe}$	0.418±0.010	0.422±0.010	$0.64^{+0.11}_{-0.08}$	$0.82^{+0.13}_{-0.10}$	keV
$A_{\rm Cyc}$	-10.4±0.7	-6.9±0.5	-2.36±0.09	0.6±0.3	
$E_{\rm Cyc}$	40.44±0.15	40.32±0.16	40.10±0.16	37.4±0.2	keV
$\sigma_{\rm Cyc}$	6.82±0.19	7.2±0.2	5.18±0.14	5.8±0.3	keV

Pulse **P**rofiles of **A**ccreting **N**eutron stars **D**eeply **A**nalysed - PPANDA

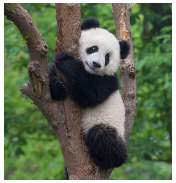

4U 1626-67 30101029002

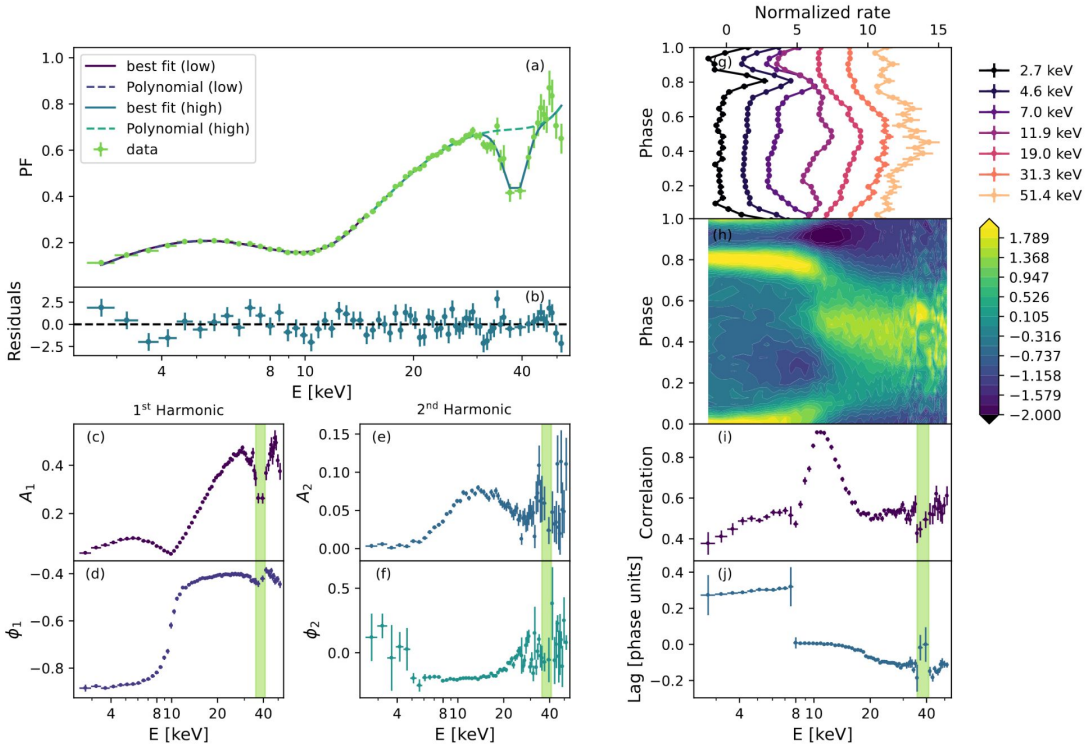

Ferrigno, D'Aì, Ambrosi, A&A, 2023

Pulse **P**rofiles of **A**ccreting **N**eutron stars **D**eeply **A**nalysed - PPANDA

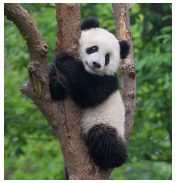

Pulsed Fraction Spectrum best-fit and residuals

full harmonic decomposition: amplitudes and phases of the harmonics

4U 1626-67 30101029002

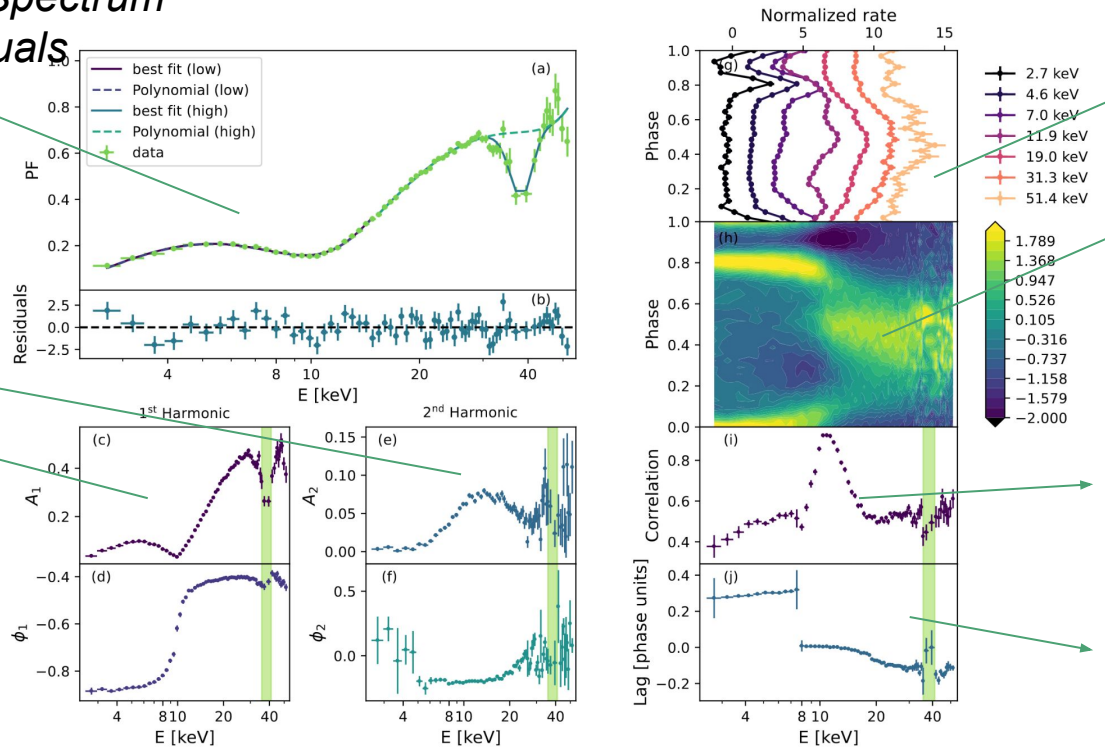

Pulse profiles

Heat map Energy-phase matrix

Correlation spectrum

Lag spectrum

Ferrigno, D'Aì, Ambrosi, A&A, 2023

Fantastic, let’s analyse all the sources with cyclotron lines !!!

Fantastic, let’s analyse all the sources with cyclotron lines !!!

Dips and bumps

Sometimes there are bumps at the Ecycl

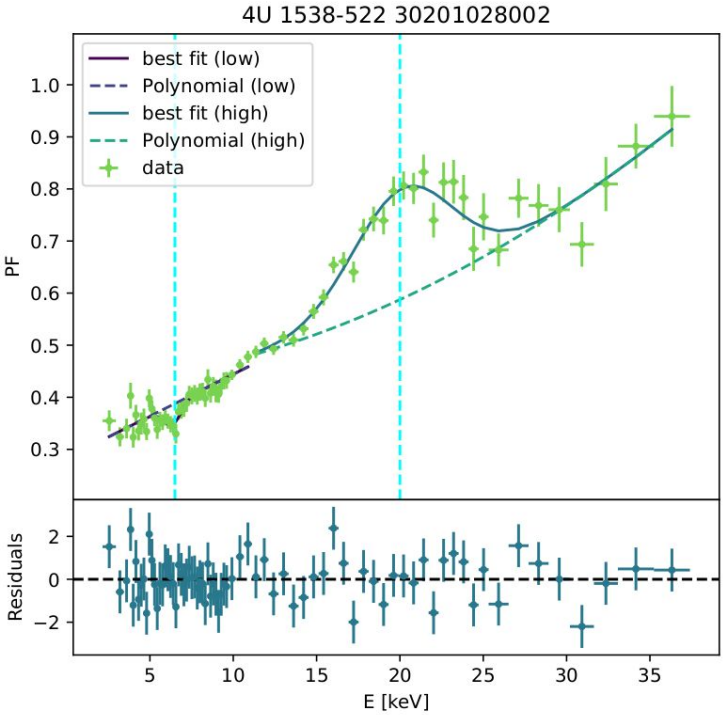

PFS: dips and bumps at the cyclotron line energy

Not a dip, but some sort of bump…

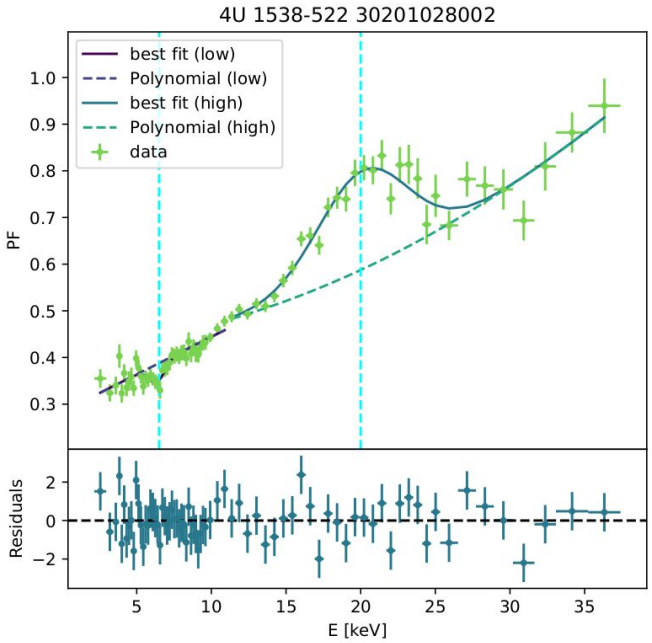

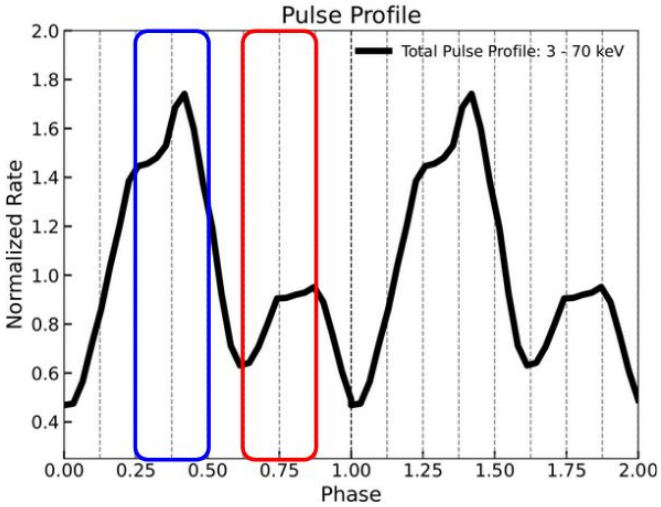

Maniadakis, Sokolova-Lapa, D'Aì et al., A&A, 2025,

How the spin-phase variability of cyclotron lines shapes the pulsed fraction spectra: Insights from 4U1538–52.

Cyclotron line energy spin dependence

Spectra of all 8 phase bins normalized at 10 keV

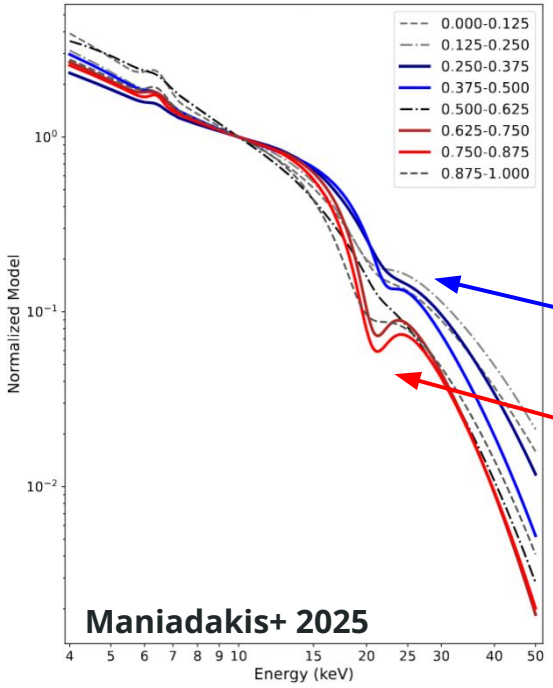

Cyclotron line parameters variation

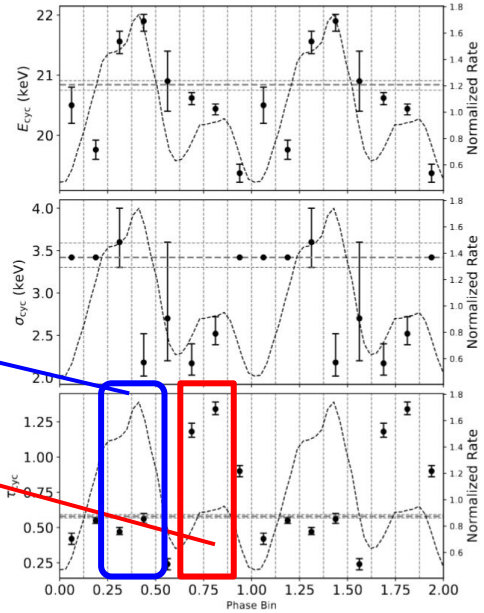

1. **CRSF deeper** at secondary peak
2. **CRSF shallower** at primary peak

Reproducing the PF features

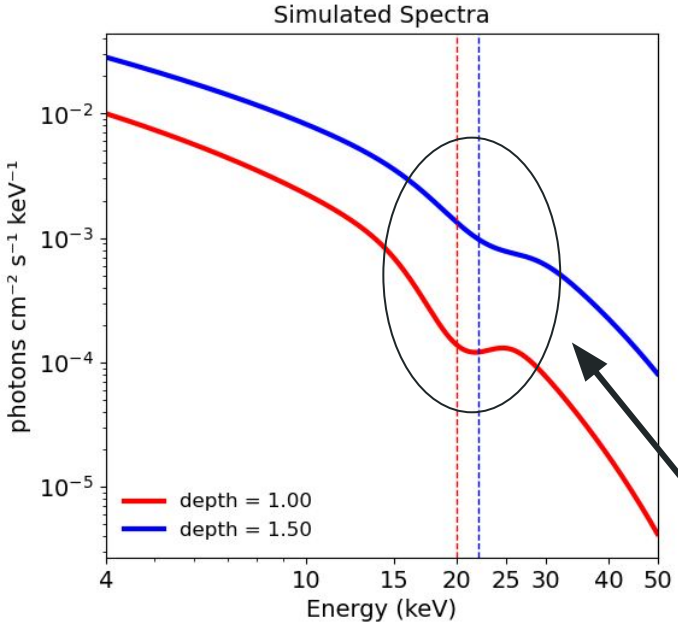

PF = σ / μ

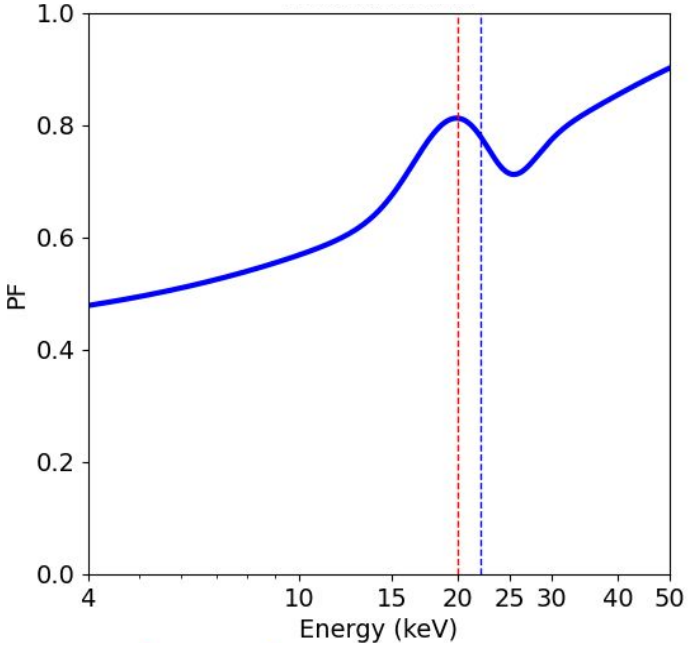

Simply said: the PF spectra track the **spectral spin variability of the Cyclotron line**

CRSF depth vs spin-dependent flux

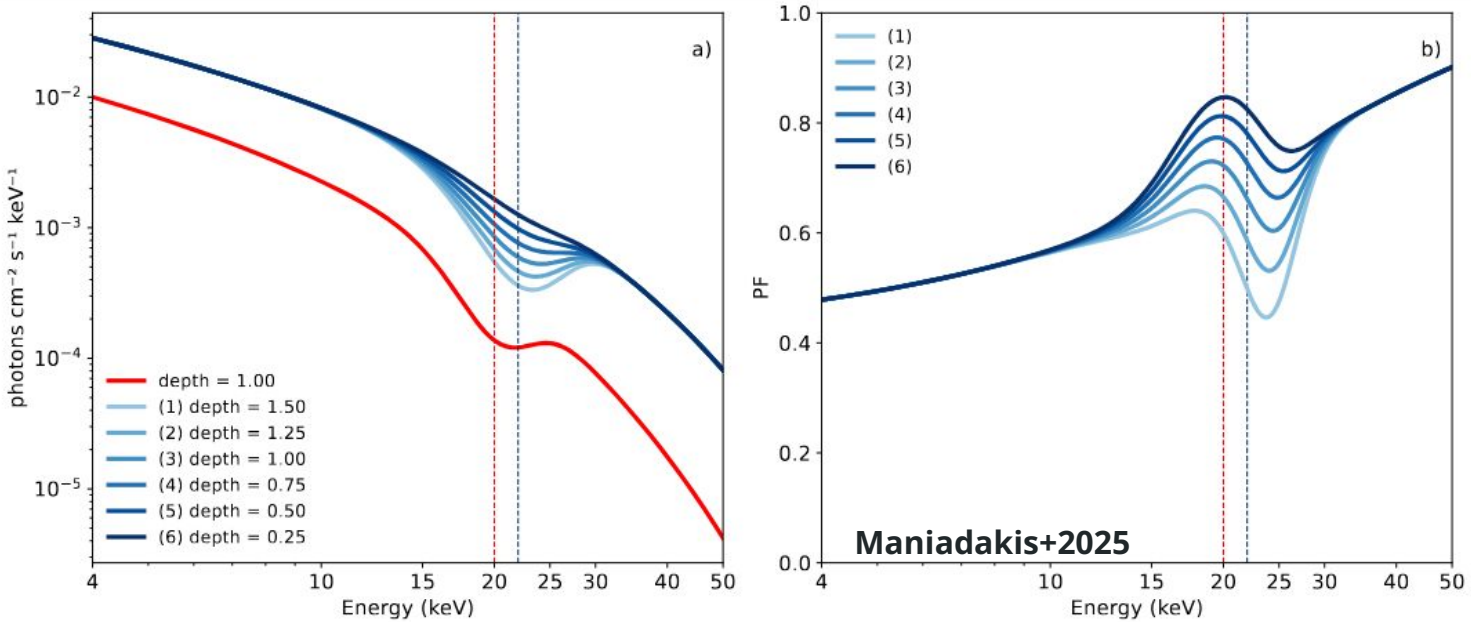

Increasing depth of the CRSF of the primary peak spectrum

Bump becomes smaller and smaller ⟶ **Dip becomes deeper and deeper**

Feature has a more **complicated shape**: the energy does not coincide with the spectral value

Uncovering state-dependent cyclotron lines

4U 1901+03 Spectra Modelling

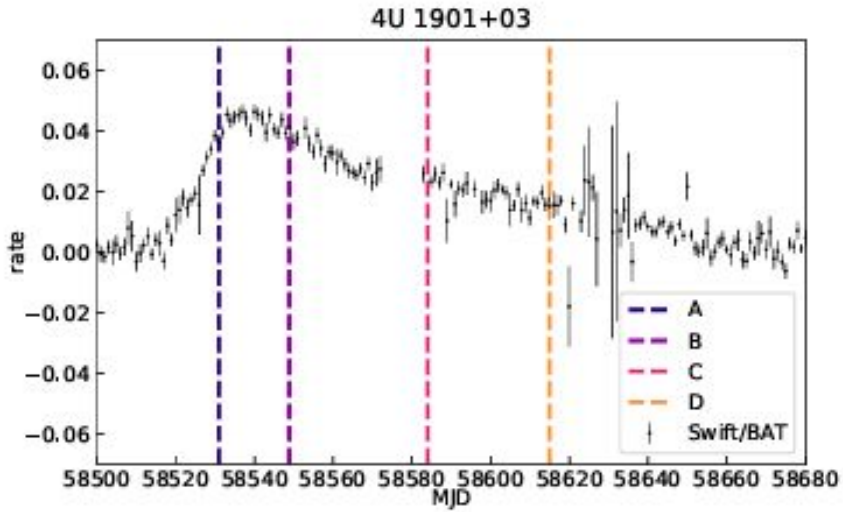

A&A 652, A89 (2021)
https://doi.org/10.1051/0004-6361/202038531

Astronomy & Astrophysics

Spectral evolution of X-ray pulsar 4U 1901+03 during the 2019 outburst based on Insight-HXMT and *NuSTAR* observations

Armin Nabizadeh[1], Sergey S. Tsygankov[1,2], Long Ji[3], Victor Doroshenko[3,2], Sergey V. Molkov[2], Youli Tuo[4], Shuang-Nan Zhang[4], Fan-Jun Lu[4], Shu Zhang[4], and Juri Poutanen[1,2,5]

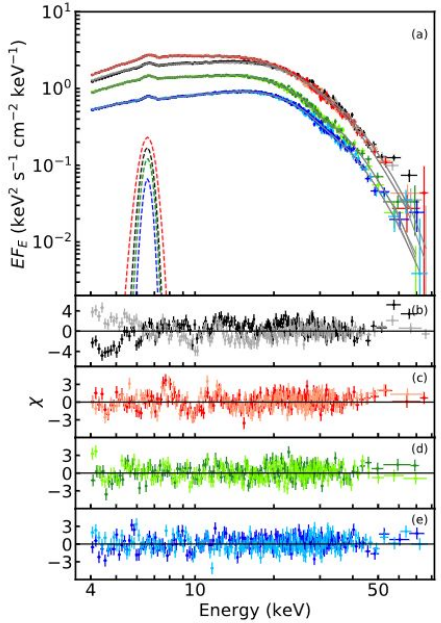

Fig. 6. Same as Fig. 2, but only for the *NuSTAR* observations together with the best-fit model (TBABS × (GAU+COMPTT × GABS × GABS)). Lighter colours represent the data obtained from the *NuSTAR*/FPMB module.

4U 1901+03 Energy Spectra Modelling

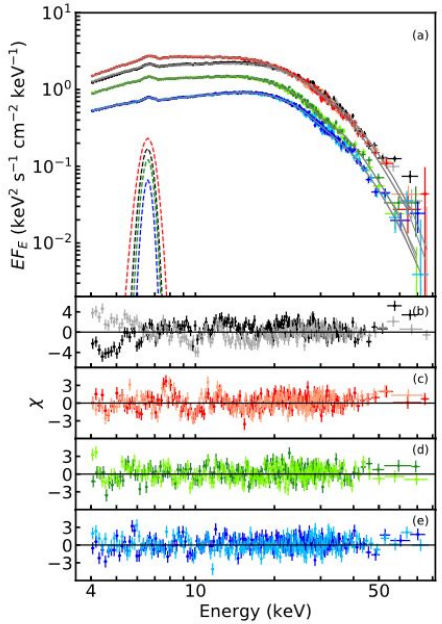

Fig. 6. Same as Fig. 2, but only for the *NuSTAR* observations together with the best-fit model (TBABS × (GAU+COMPTT × GABS × GABS)). Lighter colours represent the data obtained from the *NuSTAR*/FPMB module.

Table 3. Best-fit parameters for the model TBABS × (GAU+COMPTT × GABS × GABS) for the four data sets of pulse-averaged spectra during the 2019 outburst.

Model	Parameters	Units	NuObs1	NuObs2	NuObs3 +P0211006008	NuObs4 +P0211006022
CONSTANT [a]	FPMB/FPMA		$0.996^{+0.001}_{-0.001}$	$1.026^{+0.001}_{-0.001}$	$1.028^{+0.001}_{-0.001}$	$1.017^{+0.001}_{-0.001}$
CONSTANT [b]	LE/FPMA				$0.995^{+0.004}_{-0.004}$	$0.935^{+0.003}_{-0.003}$
CONSTANT [c]	ME/FPMA				$1.004^{+0.003}_{-0.003}$	$0.983^{+0.002}_{-0.002}$
TBABS	N_H	10^{22} cm^{-2}	$0.9^{+0.2}_{-0.2}$	$0.3^{+0.2}_{-0.2}$	$1.17^{+0.05}_{-0.05}$	$1.42^{+0.05}_{-0.05}$
COMPTT	T_0	keV	$1.08^{+0.01}_{-0.01}$	$1.24^{+0.02}_{-0.02}$	$1.01^{+0.01}_{-0.01}$	$0.88^{+0.02}_{-0.01}$
	kT	keV	$5.64^{+0.06}_{-0.06}$	$5.25^{+0.08}_{-0.09}$	$4.88^{+0.06}_{-0.05}$	$4.91^{+0.04}_{-0.04}$
	τ_p		$4.592^{+0.04}_{-0.04}$	$4.55^{+0.04}_{-0.06}$	$5.04^{+0.05}_{-0.05}$	$5.29^{+0.08}_{-0.1}$
	A_{comptt}		$0.148^{+0.002}_{-0.002}$	$0.186^{+0.002}_{-0.003}$	$0.122^{+0.002}_{-0.002}$	$0.080^{+0.004}_{-0.002}$
GABS	E_{abs1}	keV	$10.6^{+0.1}_{-0.1}$	$10.8^{+0.2}_{-0.2}$	$10.5^{+0.1}_{-0.1}$	$9.0^{+0.4}_{-0.8}$
	σ_{abs1}	keV	$1.1^{+0.2}_{-0.2}$	$1.7^{+0.2}_{-0.3}$	$2.1^{+0.2}_{-0.2}$	$4.4^{+0.8}_{-0.5}$
	τ_{abs1}		$0.03^{+0.01}_{-0.01}$	$0.05^{+0.01}_{-0.02}$	$0.06^{+0.01}_{-0.01}$	$0.14^{+0.1}_{-0.05}$
GABS	E_{abs2}	keV	$39.2^{+0.4}_{-0.4}$	$35.3^{+0.4}_{-1.4}$	$32.2^{+0.6}_{-0.6}$	$32.4^{+0.6}_{-0.5}$
	σ_{abs2}	keV	$10.0^{+3.4}_{-0.5}$	$9.9^{+2.0}_{-1.5}$	$5.8^{+0.6}_{-0.5}$	$5.5^{+0.8}_{-0.6}$
	τ_{abs2}		$0.46^{+0.19}_{-0.06}$	$0.37^{+0.2}_{-0.2}$	$0.30^{+0.09}_{-0.08}$	$0.21^{+0.09}_{-0.06}$
GAUSSIAN	E_{Fe}	keV	$6.54^{+0.01}_{-0.01}$	$6.53^{+0.01}_{-0.01}$	$6.57^{+0.01}_{-0.01}$	$6.58^{+0.01}_{-0.01}$
	σ_{Fe}	keV	$0.30^{+0.02}_{-0.02}$	$0.31^{+0.02}_{-0.02}$	$0.28^{+0.02}_{-0.02}$	$0.23^{+0.02}_{-0.02}$
	A_{Fe}	10^{-3} ph s^{-1} cm^{-2}	$3.4^{+0.2}_{-0.2}$	$5.0^{+0.3}_{-0.3}$	$2.2^{+0.1}_{-0.1}$	$0.96^{+0.05}_{-0.05}$
$F_{1-79\,keV}$ [d]		10^{-9} erg s^{-1} cm^{-2}	$7.49^{+0.03}_{-0.04}$	$8.51^{+0.05}_{-0.04}$	$4.95^{+0.01}_{-0.01}$	$3.082^{+0.009}_{-0.009}$
$F_{4-79\,keV}$ [d]		10^{-9} erg s^{-1} cm^{-2}	$6.47^{+0.02}_{-0.02}$	$7.43^{+0.03}_{-0.03}$	$4.183^{+0.006}_{-0.006}$	$2.561^{+0.003}_{-0.003}$
χ^2(d.o.f.)			2085 (1665)	1615 (1564)	2963 (2949)	3417 (3087)

Notes. [a]Cross-normalisation constant between FPMB and FMPA instruments on board *NuSTAR*. [b]Cross-normalisation constant between Insight-HXMT/LE and *NuSTAR*/FPMA instruments. [c]Cross-normalisation constant between Insight-HXMT/ME and *NuSTAR*/FPMA instruments. [d]Unabsorbed X-ray flux.

Luminosity-dependence of the PFS features

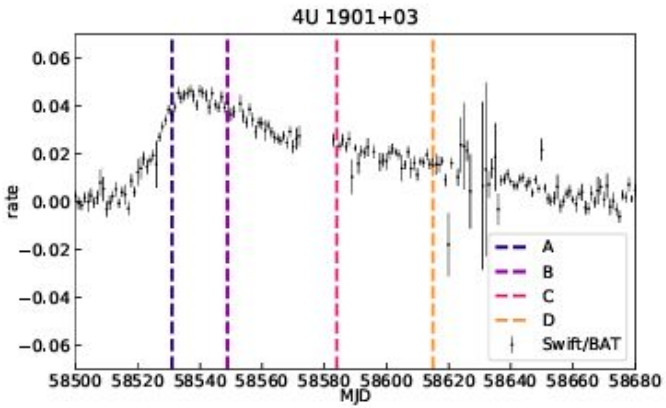

Almost featureless PFS at high Lum

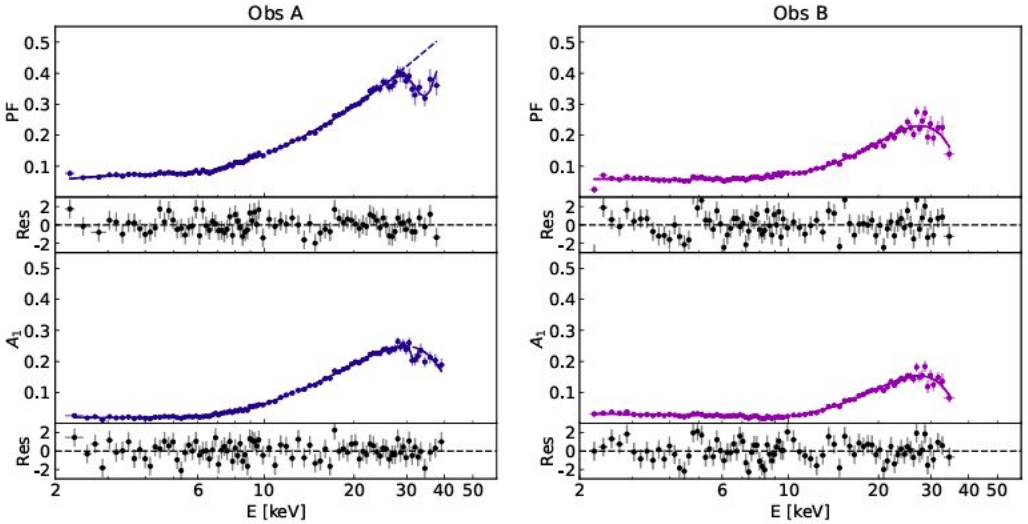

[Ambrosi, D'Aì et al, 2026, A&A]

Luminosity-dependence of the PFS features

A clear hint to a feature at low Lum

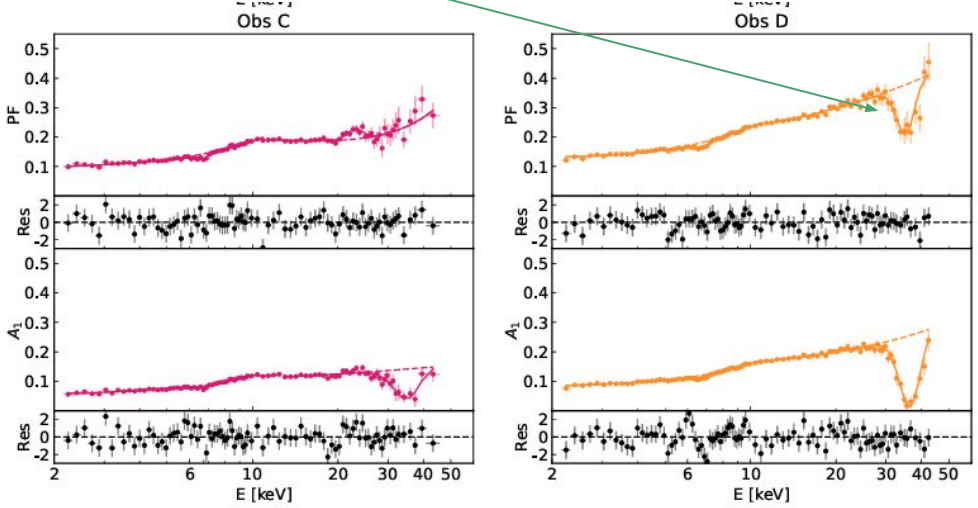

Table 4. Posterior parameter estimates for the cyclotron resonance model.

Parameter	A	B	C	D
C_{FPMB}	0.938 ± 0.003	0.988 ± 0.004	0.985 ± 0.004	0.969 ± 0.003
Γ	$-0.27^{+0.07}_{-0.08}$	0.2 ± 0.1	-0.1 ± 0.1	-0.8 ± 0.1
E_{cut} [keV]	6.2 ± 0.1	6.7 ± 0.2	6.1 ± 0.2	5.4 ± 0.1
Norm	0.057 ± 0.009	0.20 ± 0.06	0.06 ± 0.01	0.007 ± 0.002
E_{cyc},[keV]	$32.1^{+1.2}_{-0.8}$	32.2 ± 1.3	32.1 ± 0.8	31.7 ± 0.6
σ_{CRSF} [keV]	$4.5^{+1.4}_{-1.3}$	$6.0^{+0.7}_{-1.0}$	$5.2^{+0.9}_{-0.8}$	5.8 ± 0.7
$\mathrm{Depth}_{\mathrm{CRSF}}$ [keV]	$0.8^{+0.5}_{-0.3}$	$1.6^{+0.6}_{-0.5}$	$3.0^{+1.1}_{-0.8}$	$2.7^{+0.8}_{-0.6}$
$\log_{10}$BF	0.98	5.1	25.0	23.8

Notes. We report the median and 68% credible intervals (16th and 84th percentiles) for each parameter. The final row provides the log-evidence ($\log_{10}$ BF) compared to a null model.

Ambrosi, D'Aì et al, 2026, A&A

Cyclotron line wings

The PFS of V 0332+53

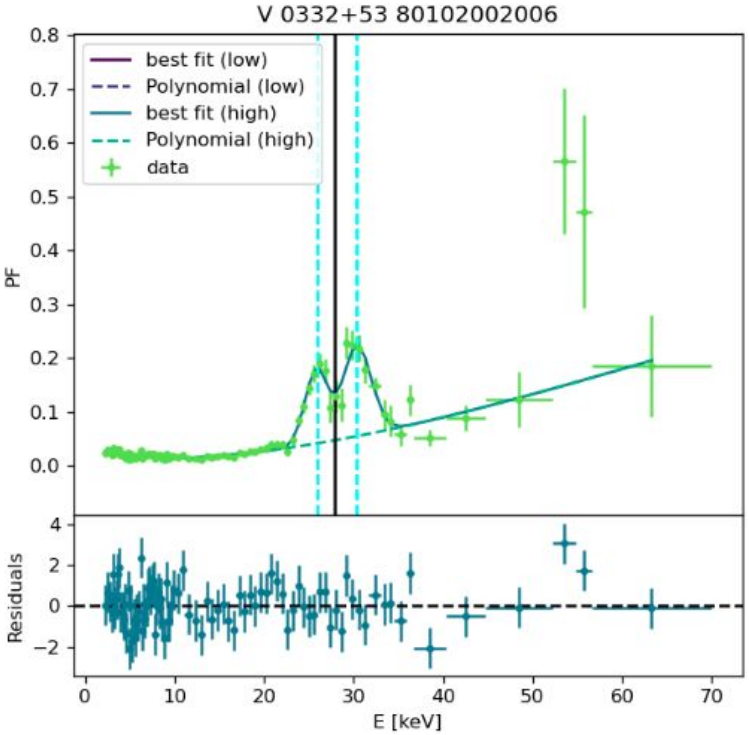

The PF spectra of V0332 from Nustar observations

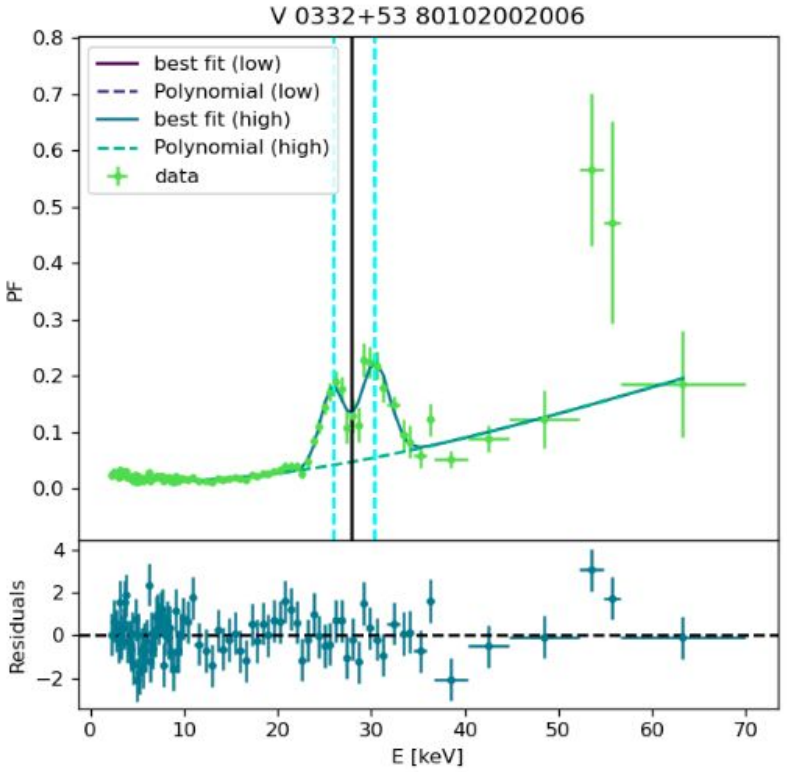

D'Aì et al., A&A, 2025

			806	
$\chi^2_{\rm red,lo}$/d.o.f.	1.0/43	1.2/43	0.9/45	—
$\chi^2_{\rm red,hi}$/d.o.f.	1.2/36	1.9/36	1.3/33	—
$n_{\rm pol}^{\rm (hi)}$	3	3	3	—
$n_{\rm pol}^{\rm (lo)}$	1	1	2	—
$E_{\rm split}$ (keV)	10.01	10.01	12.08	—
A_1	0.38±0.02	0.228±0.011	$0.28^{+0.06}_{-0.10}$	0.86
E_1 (keV)	25.78±0.08	25.81±0.06	$27.4^{+0.3}_{-0.5}$	27.93
σ_1 (keV)	1.20±0.06	1.12±0.05	$1.96^{+0.18}_{-0.22}$	8.47
A_2	0.66±0.05	0.340±0.019	$0.17^{+0.10}_{-0.05}$	—
E_2 (keV)	30.28±0.11	30.56±0.07	31^{+2}_{-2}	—
σ_2 (keV)	1.68±0.14	1.16±0.06	$2.0^{+0.5}_{-0.7}$	—
$D_{\rm cyc}$	—	—	—	0.862±0.002
$E_{\rm cyc}$ (keV)	—	—	—	28.40±0.02
$\sigma_{\rm cyc}$ (keV)	—	—	—	7.59±0.08

The PF spectra of V0332 from Nustar observations

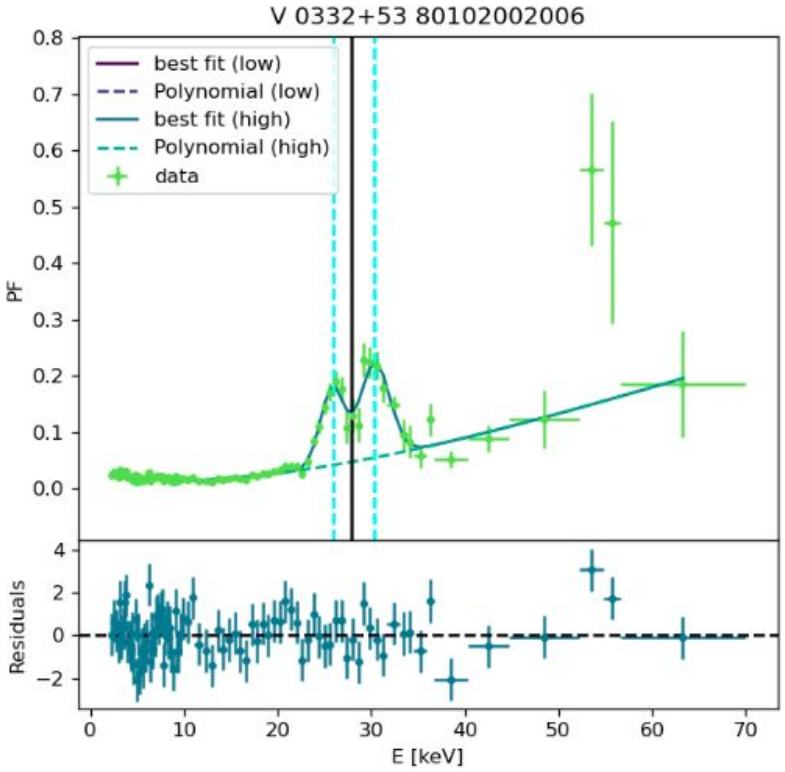

D'Aì et al., A&A, 2025

			806	
$\chi^2_{\rm red,lo}$/d.o.f.	1.0/43	1.2/43	0.9/45	—
$\chi^2_{\rm red,hi}$/d.o.f.	1.2/36	1.9/36	1.3/33	—
$n_{\rm pol}^{\rm (hi)}$	3	3	3	—
$n_{\rm pol}^{\rm (lo)}$	1	1	2	—
$E_{\rm split}$ (keV)	10.01	10.01	12.08	—
A_1	0.38±0.02	0.228±0.011	$0.28^{+0.06}_{-0.10}$	0.86
E_1 (keV)	25.78±0.08	25.81±0.06	$27.4^{+0.3}_{-0.5}$	27.93
σ_1 (keV)	1.20±0.06	1.12±0.05	$1.96^{+0.18}_{-0.22}$	8.47
A_2	0.66±0.05	0.340±0.019	$0.17^{+0.10}_{-0.05}$	—
E_2 (keV)	30.28±0.11	30.56±0.07	31^{+2}_{-2}	—
σ_2 (keV)	1.68±0.14	1.16±0.06	$2.0^{+0.5}_{-0.7}$	—
$D_{\rm cyc}$	—	—	—	0.862±0.002
$E_{\rm cyc}$ (keV)	—	—	—	28.40±0.02
$\sigma_{\rm cyc}$ (keV)	—	—	—	7.59±0.08

from the spectral analysis of Doroshenko+17

The overall picture: two peaks always at both side of Ecyc

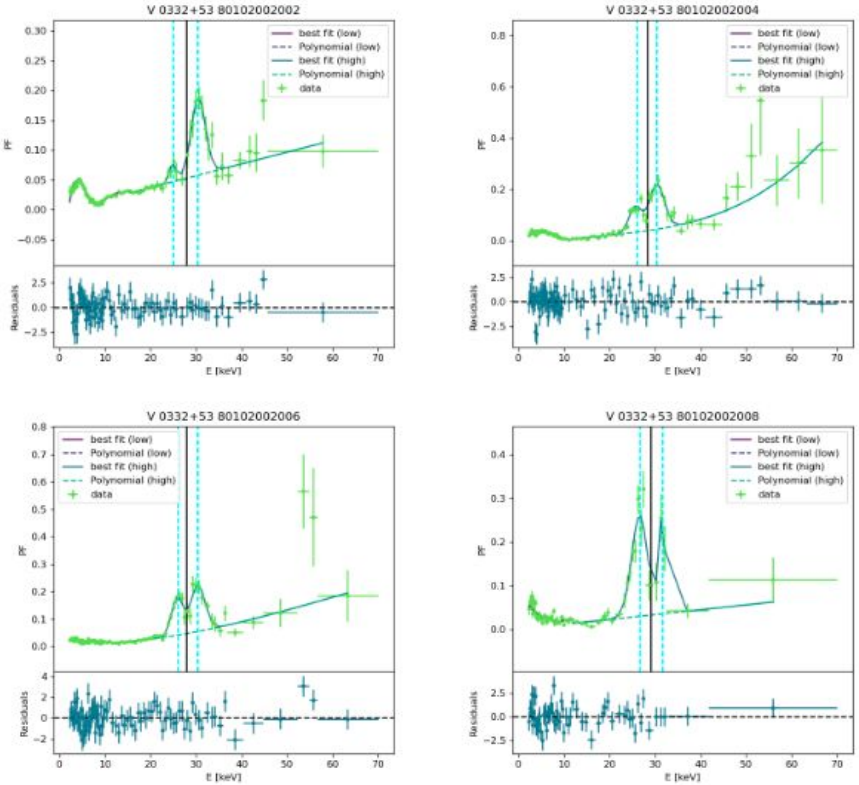

The overall picture: two peaks always at both side of Ecyc

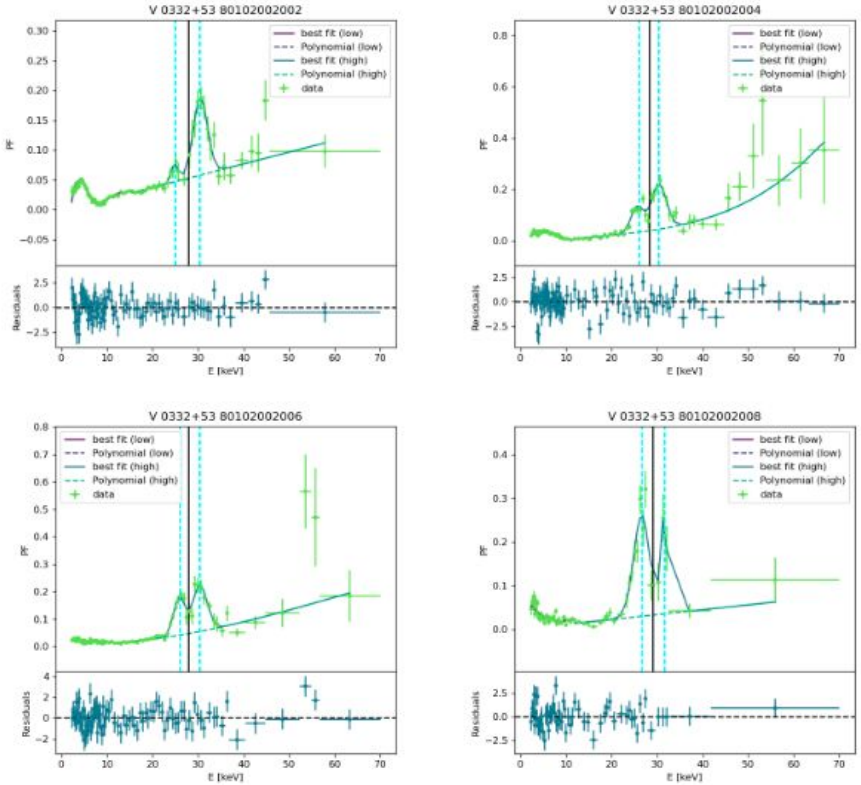

Data and best-fitting models from the first 4 obs.

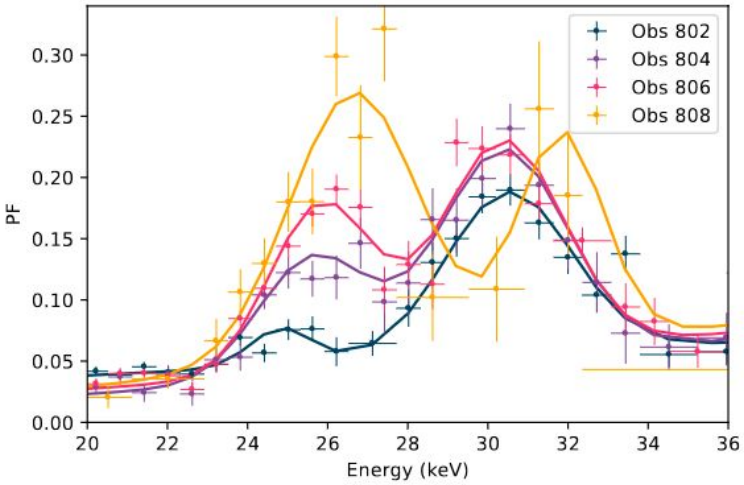

What is the origin of this variability?

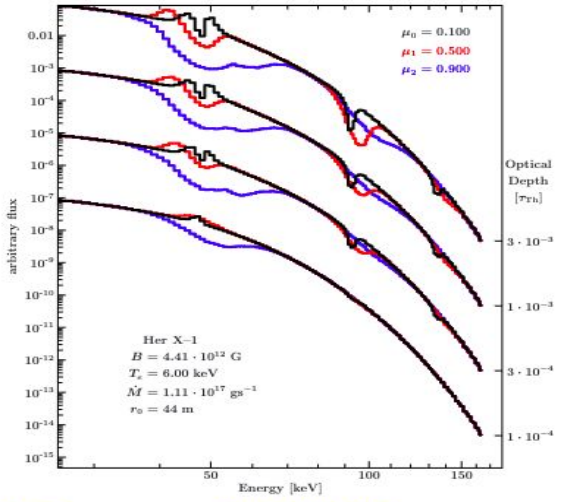

Fig. 5. Continuum from Becker & Wolff (2007) with imprinted cyclotron lines for several angles $\mu = \cos\vartheta$ to the magnetic field axis and optical depths τ. The continuum parameters are the same as in the spectrum from Becker & Wolff (2007, Fig. 6 therein) for Her X-1. The different colors show three angles to the magnetic field axis. The optical depth is increasing from the bottom to the top as shown by the axis on the right-hand side.

Schwarm+17

Cyclotron lines are (theoretically) expected to be asymmetric with broad line wings depending on the observing angle, and physical and geometrical properties of the line forming region.

The appearance of these wings is strongly indicative of a face-on geometry, with a small angle between the rotation and magnetic axis.

The low-energy landscape

Building a broadband PFS

EPIC/pn and NuSTAR cross-calibration of pulse profiles from a simultaneous observation of Vela X-1

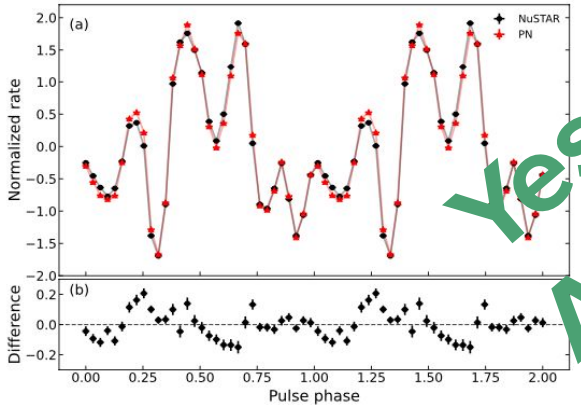

Fig. 5: (a) Pulse profiles of Vela X-1 in the 4–5 keV energy band extracted with *XMM-Newton*/EPIC-pn and *NuSTAR*, folded into 32 phase bins. (b) Phase-by-phase difference between the normalized pulse profiles derived from the two instruments.

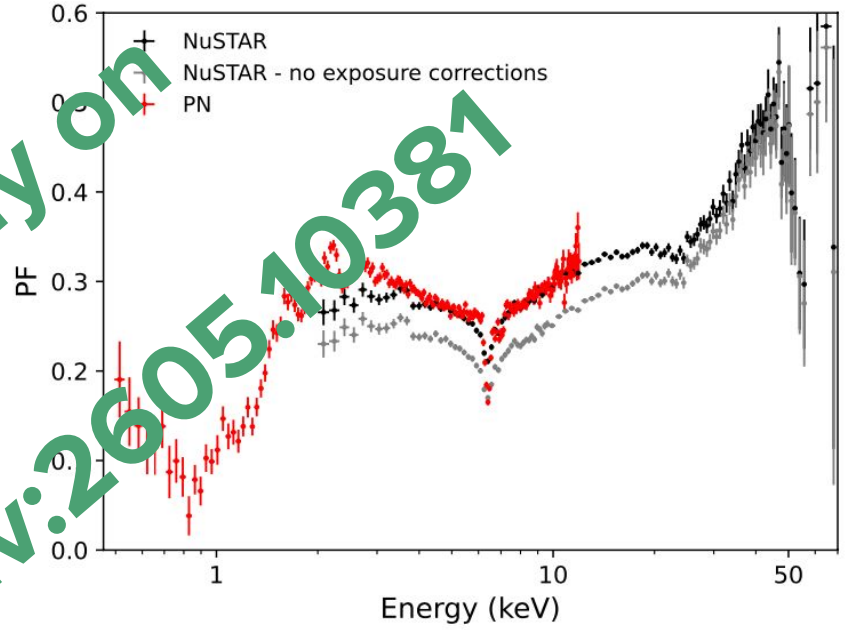

Yesterday on Arxiv ! arXiv:2605.10381

Maniadakis, D'Aì et al., A&A, 2026

Building a broadband PFS

EPIC/pn and NuSTAR cross-calibration of pulse profiles from a simultaneous observation of Vela X-1

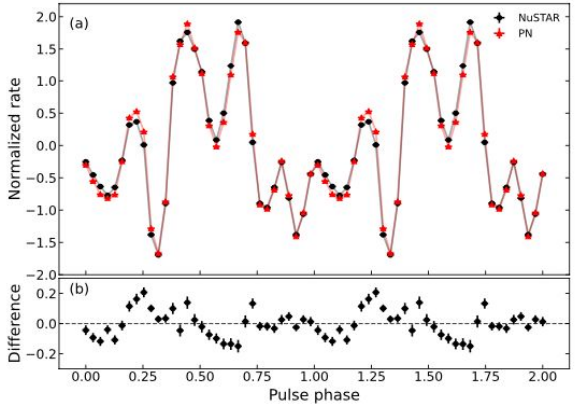

Fig. 5: (a) Pulse profiles of Vela X-1 in the 4–5 keV energy band extracted with *XMM-Newton*/EPIC-pn and *NuSTAR*, folded into 32 phase bins. (b) Phase-by-phase difference between the normalized pulse profiles derived from the two instruments.

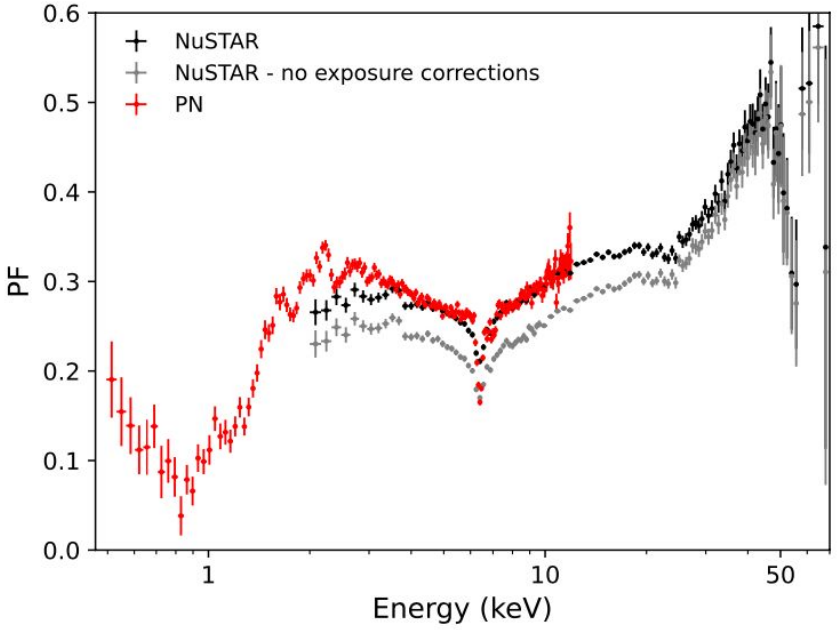

Maniadakis, D'Aì et al., A&A, 2026

The iron range landscape

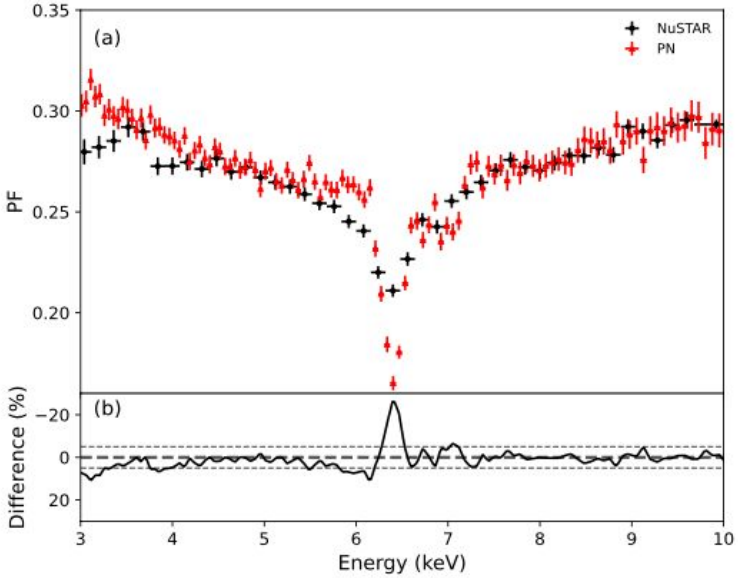

(a) Pulsed fraction spectra calculated with the rms method.

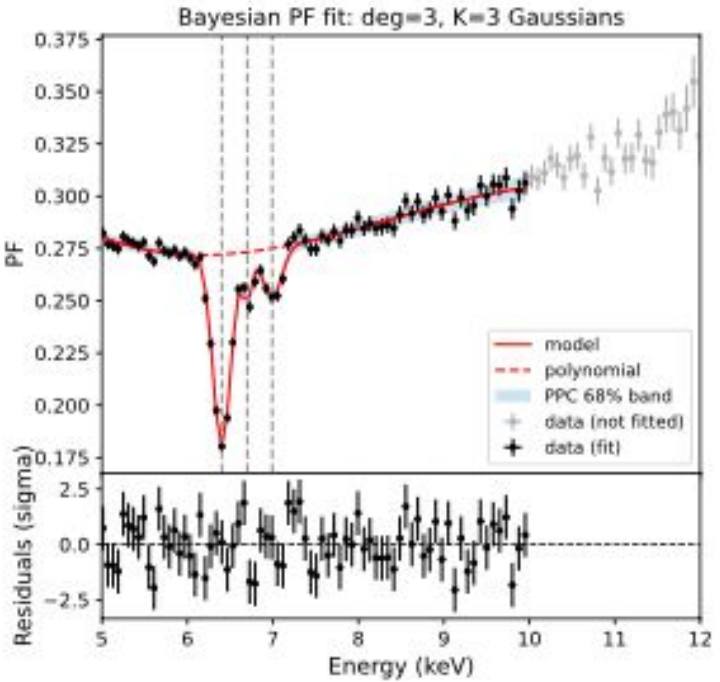

(b)

Maniadakis, D'Aì A&A 2026

The low-energy landscape of spectral features

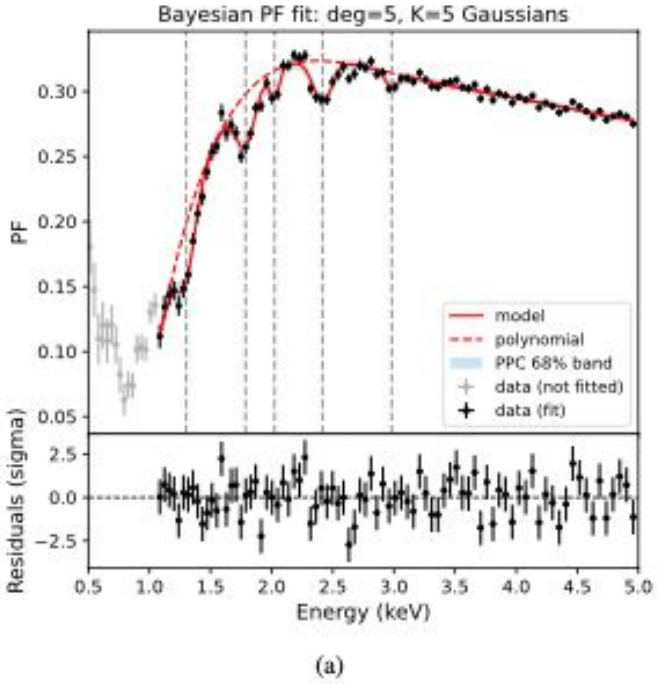

(a)

Maniadakis, D'Aì A&A 2026

Time-dependent evolution of the PFS

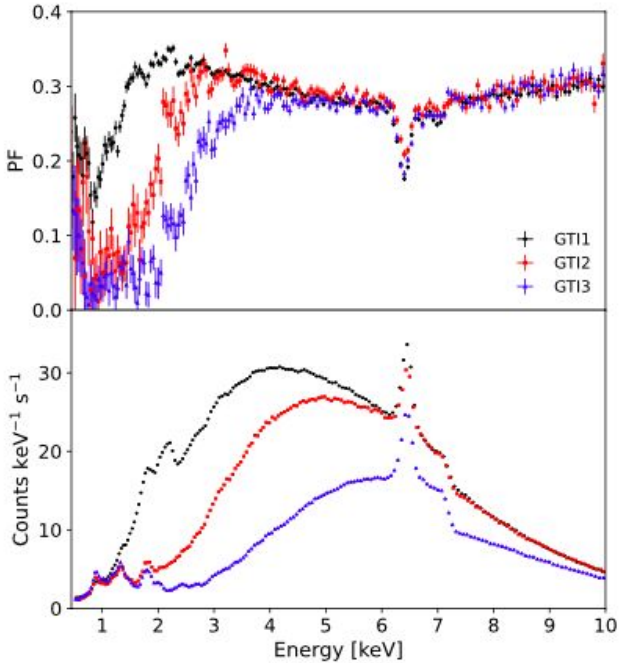

Exploiting the high resolution of XRISM

XRISM observation of Cen X-3

196 ks observation made on Feb. 12 2024, covering one complete orbit (Porb=179.7 ks)

The Astrophysical Journal Letters, 977:L21 (8pp), 2024 December 10 https://doi.org/10.3847/2041-8213/ad946d

Detection of the Orbital Modulation of Fe Kα Fluorescence Emission in Centaurus X-3 Using the High-resolution Spectrometer Resolve on board XRISM

Yuto Mochizuki[1,2], Masahiro Tsujimoto[1], Richard L. Kelley[3], Bert Vander Meulen[4], Teruaki Enoto[5], Yutaro Nagai[5], Chris Done[6], Pragati Pradhan[7], Natalie Hell[8], Katja Pottschmidt[9,10], Ken Ebisawa[1,2], and Ehud Behar[11]

9.3e6 of clean events (3.6e6 of Hp)

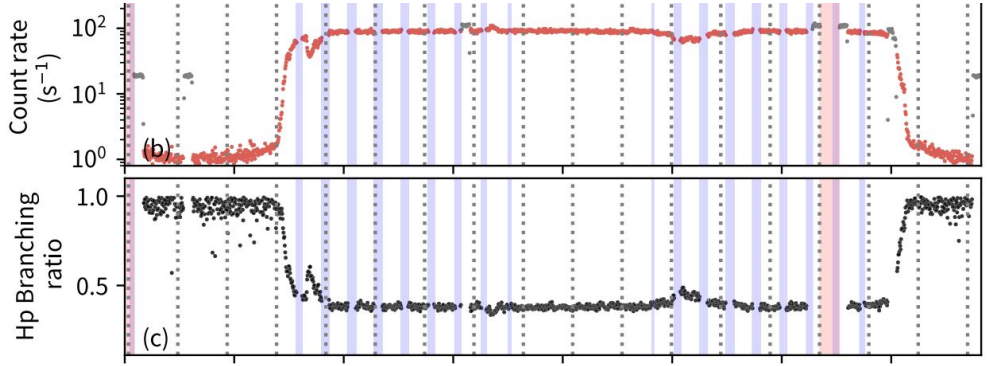

NS timing & energy resolved profiles

Mochizuki+24

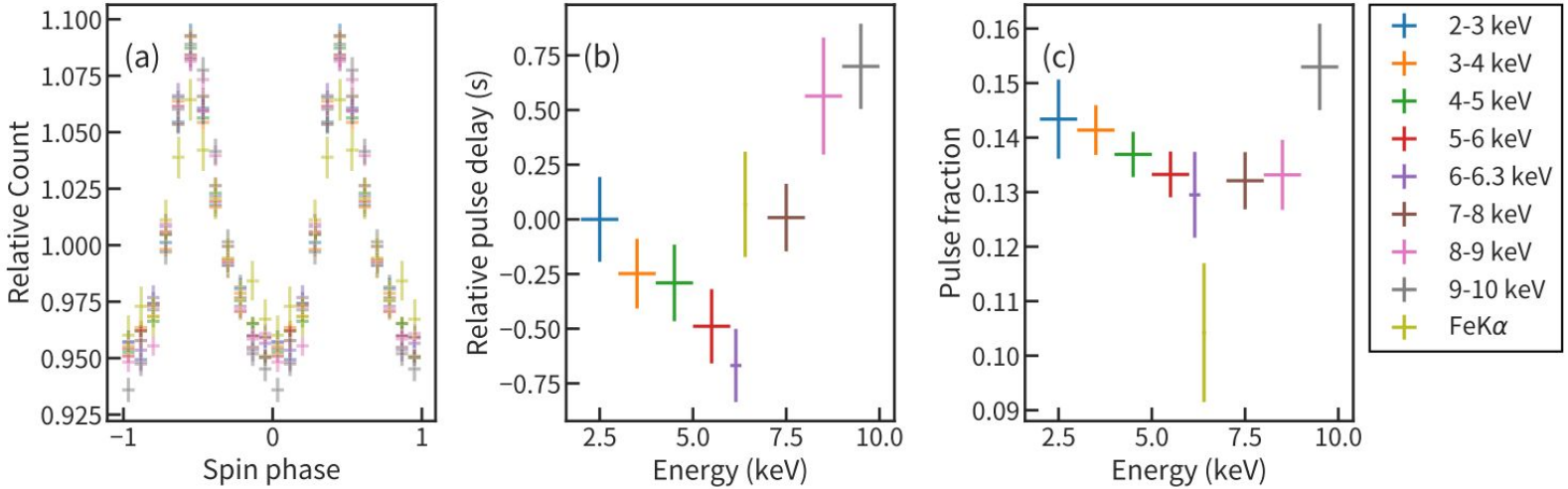

Figure 4. (a) Pulse shape folded by $P_{\rm spin}$, (b) phase delay relative to the lowest energy band as a function of energy, and (c) pulse fraction as a function of energy. The Fe Kα count rate is from 6.35 to 6.45 keV.

The 2-12 keV Resolve energy phase matrix and PFS

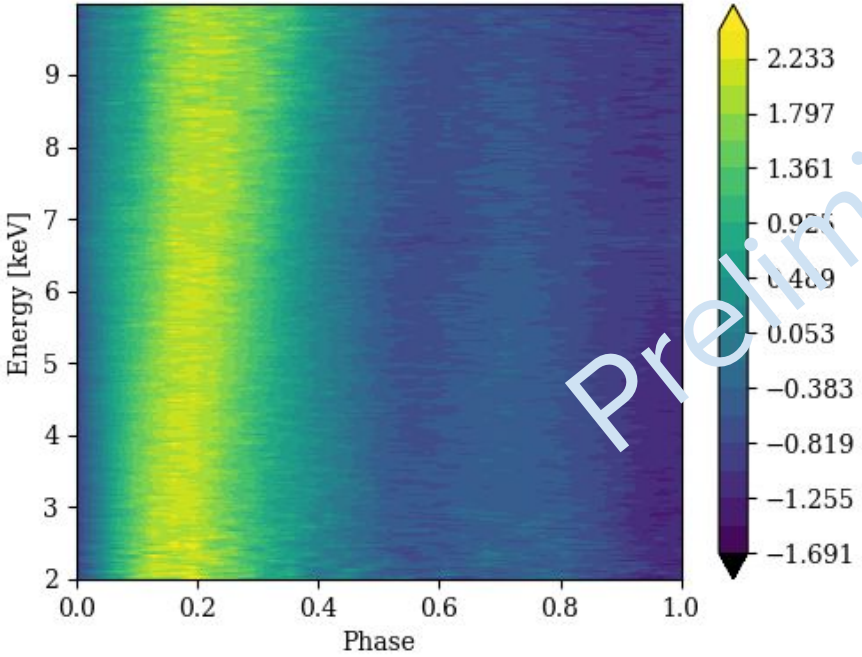

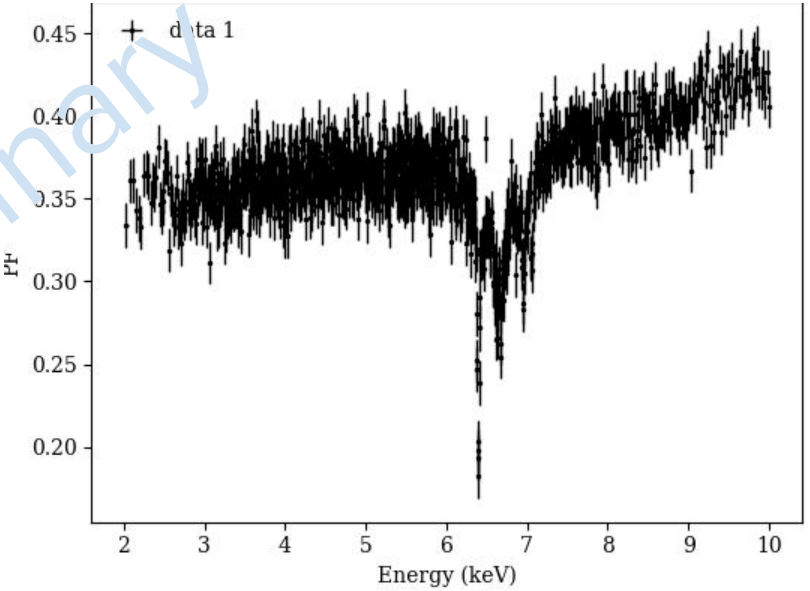

Conclusions

- Tested methodology for a large variety of cases
- Introduced flexibility for ingesting different types of detectors
- Configurable parameters for the perfect fine-tuning (choice of GTI, best signal-to-noise ratio, fit modelling and so on)
- Working on a spectral-timing approach to improve determination of spectral and timing parameters

Do you have a particular source you want to analyse? Want to join?

Contact me **antonino.dai@inaf.it**

Back-up material

Physical modeling simulations using the **FINRAD** code (Sokolova-lapa+2021,2023)

We **reproduce the observables**, using the ***FINRAD*** code (Radiative Transfer Equation for two hotspots in NS)

Simulated total **pulse profile**

Energy resolved pulse profile around the **CRSF** energy

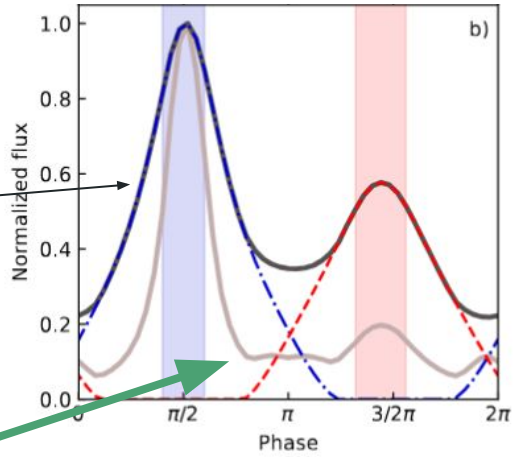

Simulated Primary and **secondary** peak spectra

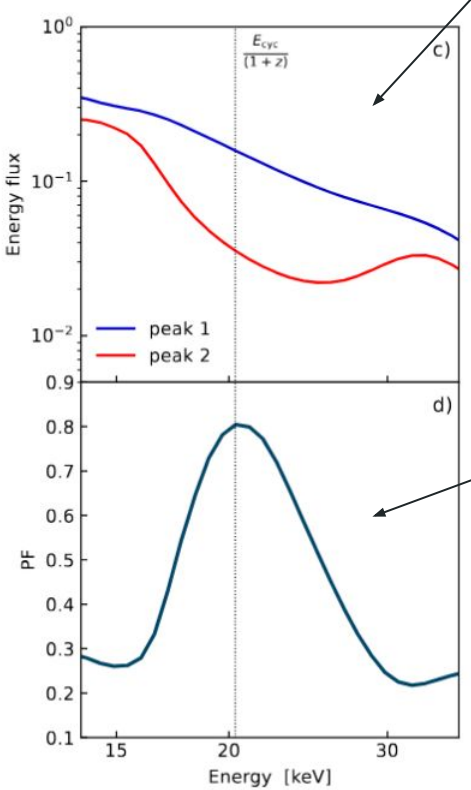

Reproducing the **bump** at the PF spectrum

Maniadakis+ 2025

Resulting Geometry of 4U 1538

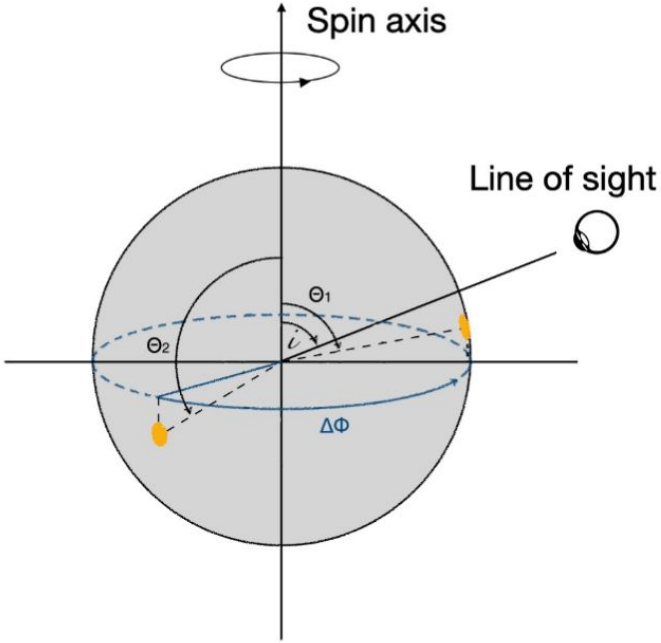

Fig. 14: Geometry adopted for 4U 1538-52, showing the neutron star, magnetic poles at $\Theta_1 = 80°$ and $\Theta_2 = 105°$, azimuthal separation $\Delta\Phi = 168°$, and inclination to the observer's line of sight $i = 67°$.

Maniadakis+ 2025

Primary vs Secondary peak

Primary peak:
- Higher flux
- **Smaller** cyclotron cross section

Secondary peak:
- Lower flux
- **Higher** cyclotron cross section

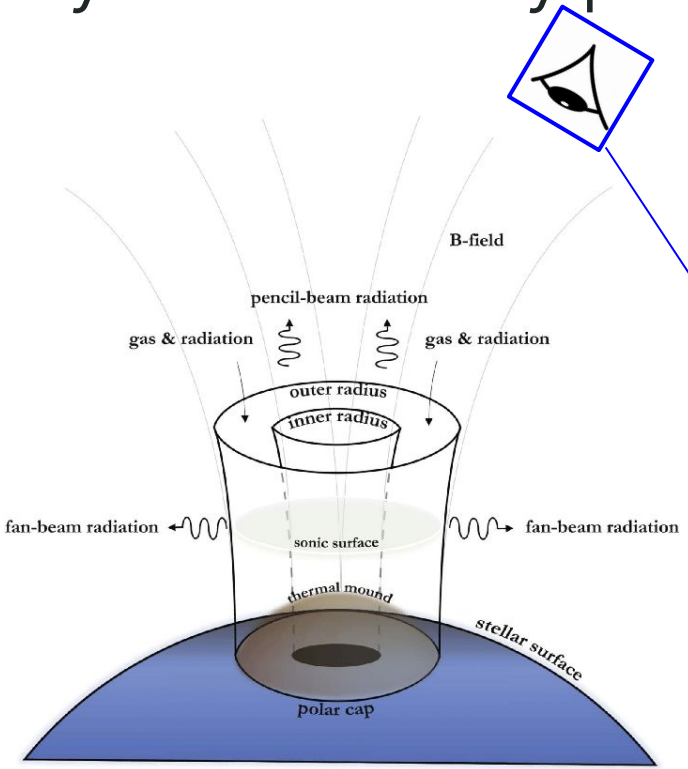

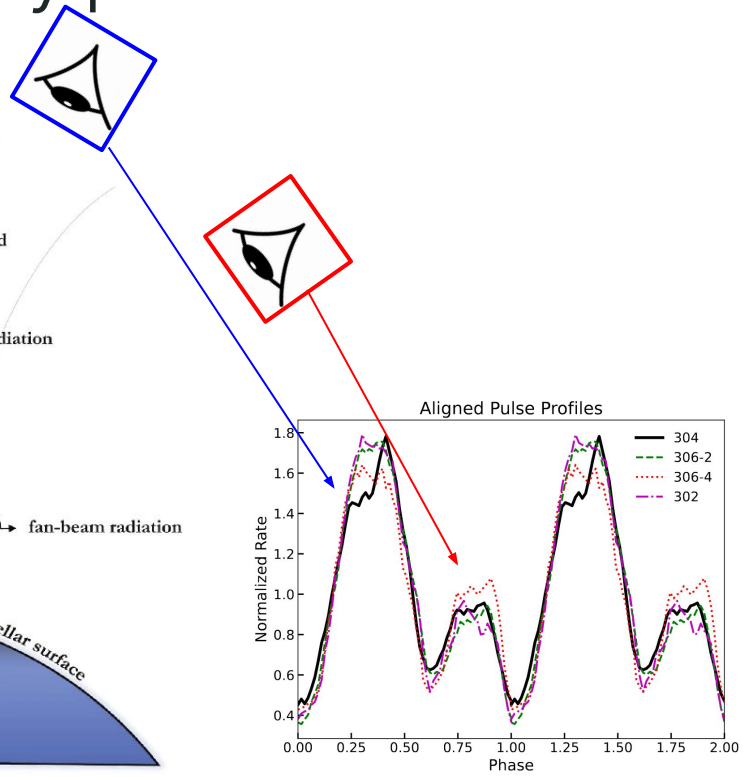

Energy range: 1 - 5 keV: EPIC-pn data / Bayesian fitting

Gaussian priors:
- centroid energies
- widths of lines: energy resolution

- Mg XI (f,i,r): E_{ref} = 1.338 keV → E_{pf} = 1.30 ± 0.01 keV
- Si XIII (f,i,r): E_{ref} = 1.823 keV →E_{pf} = 1.79 ± 0.01 keV
- Si XIV Lyα: E_{ref} = 2.0049 keV → E_{pf} = 2.01 ± 0.02 keV
- S XV (f,i,r): E_{ref} = 2.439 keV → E_{pf} = 2.41 ± 0.01 keV
- S XVI Lyα: E_{ref} = 2.6207 keV → E_{pf} = 2.63 ± 0.03 keV
- Ar VI–IX: E_{ref} = 2.9661 keV → E_{pf} = 2.98 ± 0.02 keV

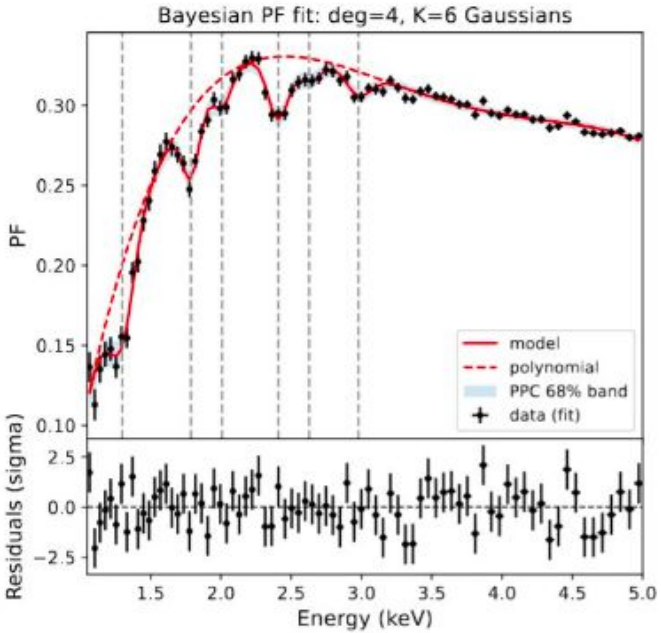

Energy range: 5 - 10 keV: EPIC-pn data / Bayesian fitting

We use all exposure this time...

There are indications in previous works for the Fe XXV triplet at ~6.7 keV (Amato+2021, Diez+2025).

- Fe Kα: E_{ref} = 6.4 keV → E_{pf} = 6.399 ± 0.005 keV
- Fe XXV: E_{ref} = 6.7 keV → E_{pf} = 6.73 ± 0.03 keV
- Fe Kβ: Eref = 7.06 keV → E_{pf} = 7.01 ± 0.02 keV

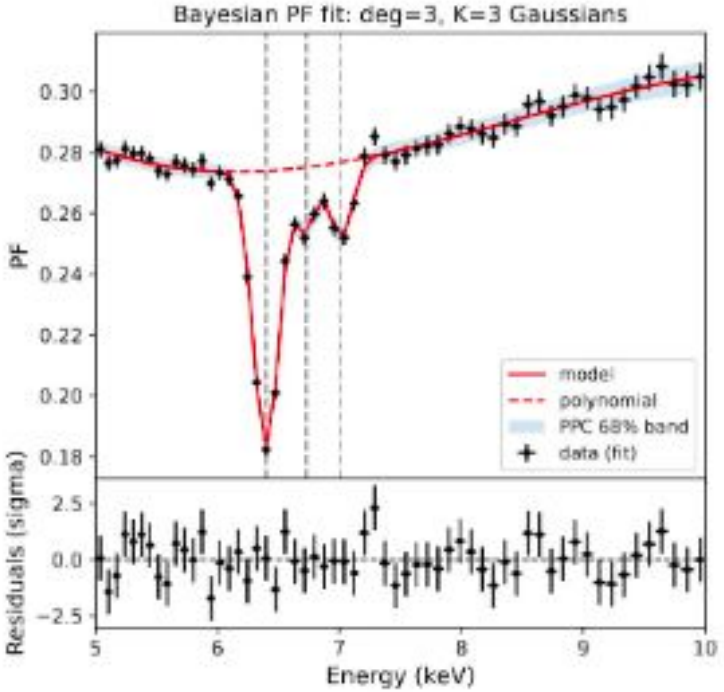

Looking for spectral counterparts

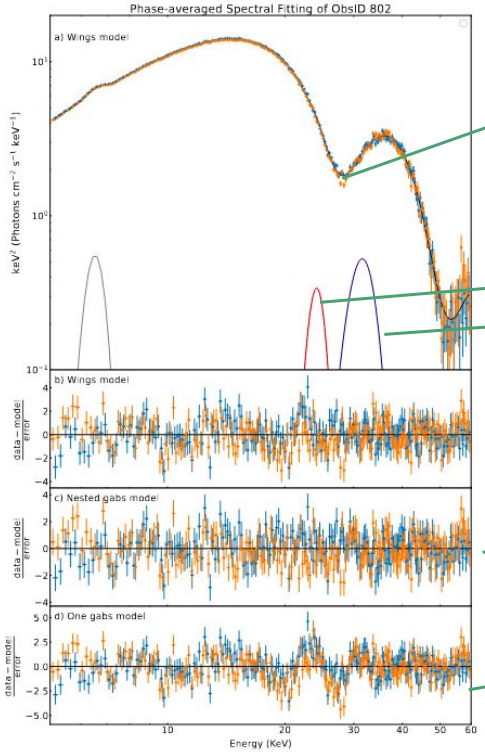

A single broad absorption feature dominates the residuals at the Ecyc

Two emission components at both sides of the cyclotron line

equivalent to a “nested” model of two abs. features of different widths

but significantly better than a single Gaussian in absorption

What if the line lags behind the continuum?